RSC Advances

ROYAL SOCIETY OF CHEMISTRY

PAPER

View Article Online
View Journal | View Issue

Cite this: *RSC Adv.*, 2026, **16**, 23987

Synthesis, cholinesterase/MAO-A inhibition, antioxidant potential and detailed computational analysis of 3,5-difluorobenzenesulfonate-tagged ethoxyvanillin hydrazones

Arooj Fatima,[a] Faiqa Noreen,[a] Halil Şenol,[b] Parham Taslimi,[c] Mostafa A. Ismail,[d] Rima D. Alharthy,[e] Asif Rasool,[f] Magdi E. A. Zaki,[g] Sobhi M. Gomha *[h] and Zahid Shafiq *[a]

A new series of hydrazones were prepared and assessed for their inhibitory activity against acetylcholinesterase (AChE), butyrylcholinesterase (BChE), and monoamine oxidase-A (MAO-A) along with their antioxidant activity. Among the tested compounds, **5i** displayed the maximum inhibitory activity with IC_{50} = 11.29 ± 0.98 nM for AChE, IC_{50} = 1.12 ± 0.41 nM for BChE, and IC_{50} = 102.70 ± 5.26 nM for MAO-A. Notably, compound **5i** was found to be more potent than the standard. Additionally, the IC_{50} values obtained from antioxidant assays ranged from 9.22 ± 0.91 nM to 19.48 ± 0.05 nM, indicating the strong free-radical scavenging property. Structure–activity relationship (SAR) studies proved that electron-withdrawing substituents play a pivotal role in increasing the inhibitory efficiency and antioxidant capacity. To validate these results, molecular docking and dynamics studies were conducted to investigate the binding contacts and possible inhibition mechanisms in the active sites of the enzyme. DFT, GCR descriptors, and ESP analyses elucidated the electronic features governing the activity. The compounds exhibited moderate cytotoxicity in HUVEC cells, with IC_{50} values ranging from 35.94 to 64.27 μM, indicating a favorable safety profile within the tested concentration range. The outcomes highlighted the substantial multifunctional potential of the evaluated hydrazones as AChE, BChE, and MAO-A inhibitors with complementary antioxidant activity, and cytotoxicity results indicated their potential for further advancement in the management of neurodegenerative conditions.

Received 6th February 2026
Accepted 15th April 2026

DOI: 10.1039/d6ra01071g

rsc.li/rsc-advances

1. Introduction

Alzheimer's disease (AD) refers to a degenerative disorder of the central nervous system and is the major cause of dementia. It is characterized by the early stages of cognitive decline and the apparent change of behavior, mostly influencing people in middle and old age.[1,2] Alzheimer's disease is not completely curable and unmanageable.[3] In a recent study, it has been referred to as Type-3 diabetes, as it is similar to diabetes in molecular and cellular operations, especially memory loss, cognitive inability, and insulin resistance, among the elderly people.[4–6]

Acetylcholinesterase (AChE) and butyrylcholinesterase (BChE) are two of the primary cholinesterase (ChE) enzymes implicated in controlling cholinergic neurotransmission by degrading acetylcholine.[7] AChE, consisting of several subunits, is highly abundant in the brain, muscles and cholinergic neurons, while BChE is predominantly expressed in neuroglial cells, which means that it can be found in organs, such as the liver, kidneys, lungs, heart, and intestines, and even in blood. In patients with Alzheimer's disease, the brain normally experiences increased BChE activity, while the action of AChE either remains constant or decreases. This leads to the conclusion that the agents that can block both the enzymes have the potential to yield superior therapeutic results compared with the agents that can block only one enzyme. Despite the structural overlap of AChE and BChE, which is estimated to be about 70 percent, the

[a]*Institute of Chemical Sciences, Bahauddin Zakariya University, Multan-60800, Pakistan*

[b]*Department of Pharmaceutical Chemistry, Faculty of Pharmacy, Bezmialem Vakif University, 34093 Fatih, Istanbul, Turkiye. E-mail: zahidshafiq@bzu.edu.pk*

[c]*Department of Biotechnology, Faculty of Science, Bartin University, 74110 Bartin, Turkiye*

[d]*Research Center for Advanced Materials Science (RCAMS), Chemistry Department, Faculty of Science, King Khalid University, P. O. Box 960, Abha 61413, Saudi Arabia*

[e]*Department of Chemistry, Science & Arts College, Rabigh Branch, King Abdulaziz University, Rabigh 21911, Saudi Arabia*

[f]*School of Chemistry and Chemical Engineering Nanjing University, Nanjing 210093, China*

[g]*Department of Chemistry, Faculty of Science, Imam Mohammad Ibn Saud Islamic University (IMSIU), Riyadh 11623, Saudi Arabia*

[h]*Department of Chemistry, Faculty of Science, Islamic University of Madinah, Madinah, 42351, Saudi Arabia. E-mail: smgomha@iu.edu.sa*

two molecules differ in terms of their three-dimensional architectures.[8]

Monoamine oxidase A (MAO-A) is an oxidoreductase enzyme which oxidatively deaminates the xenobiotic and biogenic amines.[9] It shows a strong affinity towards neurotransmitters, such as serotonin and norepinephrine. Clorgyline, a selective MAO-A inhibitor, is primarily active in catecholaminergic neurons located in the cerebral cortex.[10] MAO-A has also been known to have neuroprotective effects since it reduces the amount of hydrogen peroxide and aldehyde compounds that trigger cell destruction in the neurons.[11] The elevated levels of this enzyme are found in the heart, adipose tissues, and fat skin fibroblasts.[12]

Hydrazones act as antioxidants mainly due to their chelating properties with regard to metals. Their ability to bind with metal ions (Fe^{2+} and Cu^{2+}) inhibits the generation of reactive oxygen species (ROS), which have the potential to cause cell loss due to Fenton-type reactions.[13] Hydrazones have the ability to provide LPO and oxidative stress protection by blocking the metal ions that cause this condition of the cells. Some of the hydrazone derivatives can also scavenge free radicals directly, and hence, they are useful in the treatment of diseases associated with oxidative stress, including cancer[14,15] and neurodegenerative conditions.[16,17] Hydrazones also have well-documented diverse biological activities, including α-amylase[18] inhibition, antimicrobial,[19,20] antibacterial,[21] antitubercular,[22] cytotoxic,[23] antifungal,[24,25] antiparasitic,[26] and anticonvulsant effects.[27] They also possess enzyme inhibitory effects[28,29] and positive effects on the cardiovascular system as well as analgesic, anti-inflammatory and antiplatelet properties.[30]

Synthetic cholinesterase including tacrine, donepezil, rivastigmine, and galantamine have been used in the clinical management of Alzheimer's disease (AD). However, their application is limited by low efficiency and side effects accompanied by hepatotoxicity and gastrointestinal discomfort.[7] MAO-A inhibitors such as iproniazid, clorgyline and moclobemide exhibit energizing and anxiolytic effects. Tricyclic antidepressants[31] (tranylcypromine) continue to be a staple treatment option in regard to depression.[32] Some hydrazone and sulfonate based cholinesterase inhibitors are reported in (Fig. 1). Other treatments explored encompass AChE, BChE, and MAO-A inhibitors and those that have antioxidant and metal-chelating abilities.[18,33–37]

Phenolic compounds react with sulfonyl chlorides to produce an aryl sulfonate derivative, which is a commonly accepted intermediate in the preparation of medicines and organic synthesis.[38–42] One study published that the hydrazone derivative possessing aryl sulfonate groups exhibits potential cholinesterase inhibitory effects.[31] Molecular hybridization is a drug design approach that creates a single compound capable of acting on multiple targets involved in complex diseases.[43,44] Towards this end, hydrazones that feature 2-ethoxy-6-formylphenyl 3,5-difluorobenzenesulfonate were prepared by condensing various derivatives of hydrazides.[45,46]

Computational approaches are indispensable in modern drug discovery, providing rapid insights into ligand–target interactions and binding stability. Techniques such as molecular docking, molecular dynamics simulations and molecular

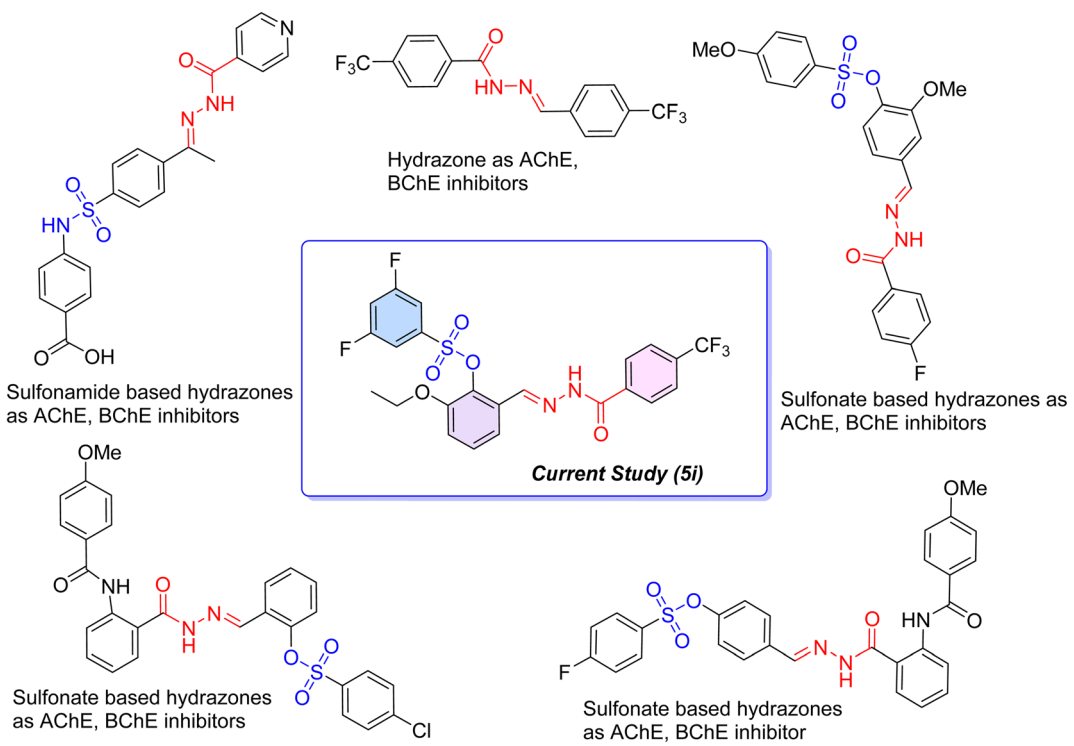

Fig. 1 Some reported hydrazone compounds with sulfonate esters as ChE inhibitors.

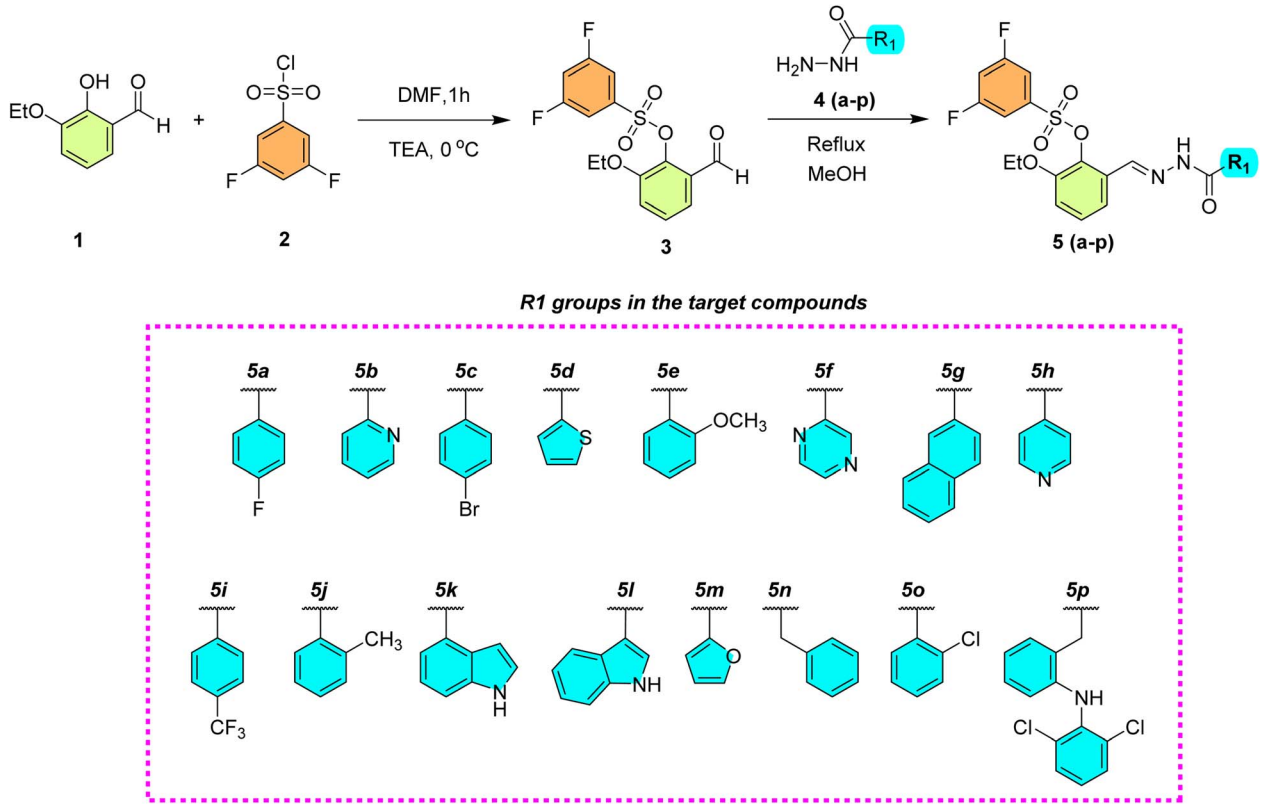

Scheme 1 Synthesis of the hydrazone derivatives 5a–5p.

mechanics with generalized Born and surface area (MM–GBSA) solvation calculations help predict affinity and conformational behavior, while density functional theory (DFT), global chemical reactivity (GCR) descriptors, and electrostatic potential (ESP) analyses reveal electronic properties that govern activity. Together, these methods enable the rational structure–activity interpretation and mechanism-guided design of new therapeutics.

The aim of this study was to design, synthesize, and biologically evaluate a new series of 3,5-difluorobenzenesulfonate-tagged ethoxyvanillin hydrazones as multifunctional agents targeting AChE, BChE, and MAO-A, along with antioxidant activities. Furthermore, comprehensive *in silico* investigations were conducted to elucidate their binding behavior, stability, and electronic features, providing mechanistic insights into their multitarget inhibitory potential for neurodegenerative disorder management.

2. Results and discussion

2.1. Chemistry

A series of compounds **5(a–p)** were synthesized by varying the –OH group of 3-ethoxysalicylaldehyde. By changing the hydroxyl moiety of 3-ethoxysalicylaldehyde (**1**) with 3,5-difluorobenzenesulfonyl chloride (**2**) using triethylamine as the catalyst at 0 °C for 1 h, 2-ethoxy-6-formylphenyl 3,5-difluorobenzenesulfonate (**3**) was synthesized. Furthermore, hydrazone derivatives **5(a–p)** were synthesized by reacting 2-ethoxy-6-formylphenyl 3,5-difluorobenzenesulfonate (**3**) with various substituted hydrazones **4(a–p)**. The pathway for the synthesis of 2-ethoxy-6-formylphenyl 3,5-difluorobenzenesulfonate-derived hydrazones **5(a–p)** is illustrated in Scheme 1.

2.2. Inhibition results of AChE, BChE, MAO-A and antioxidants (metal chelating)

Compounds with label **5(a–p)** were also produced and tested based on their ability to treat Alzheimer's disease. Table 1 shows the IC_{50} values of these compounds. The reaction of (**3**) and substituted hydrazides **4(a–p)** gave a wide variety of structurally diverse products. The presence of functional groups like phenyl and indole in the hydrazide moiety is essential in determining the structure–activity relationship as seen.

2.3. Structure–activity relationship (SAR)

2.3.1 Acetylcholinesterase (AChE). The inhibitory strength was determined by optimizing the R group on the hydrazide moiety to produce the synthesized hydrazone derivatives. These compounds exhibited better potency between (IC_{50} = 11.29 ± 0.98 nM to 36.76 ± 4.05 nM) compared to standard anti-Alzheimer drug galantamine (IC_{50} = 56.77 ± 1.26 nM). The strongest inhibition was revealed for compound **5i** (IC_{50} = 11.29 ± 0.98 nM) and the lowest one for **5c** (IC_{50} = 36.76 ± 4.05 nM). The other derivatives including the naphthalene-based **5g** (IC_{50} = 14.65 ± 1.03 nM), pyridine-based **5b** (IC_{50} = 18.47 ± 1.57 nM), indole-based **5k** (IC_{50} = 15.47 ± 1.06 nM), and thiophene-based

Table 1 IC_{50} values of the synthesized compounds against AChE, BChE, MAO-A and antioxidants

	IC_{50} (nM)			
Code	AChE	BChE	MAO-A	Metal chelating
5a	15.62 ± 1.98	1.64 ± 0.15	94.20 ± 5.57	11.27 ± 0.01
5b	18.47 ± 1.57	2.16 ± 0.26	423.01 ± 8.11	19.48 ± 0.05
5c	36.76 ± 4.05	4.17 ± 0.04	260.24 ± 6.05	15.53 ± 0.08
5d	15.31 ± 1.34	4.62 ± 0.58	504.76 ± 4.03	18.03 ± 0.05
5e	14.39 ± 2.07	3.10 ± 0.17	110.13 ± 7.21	10.68 ± 0.07
5f	13.07 ± 1.52	8.24 ± 0.40	551.53 ± 5.06	14.50 ± 0.45
5g	14.65 ± 1.03	4.42 ± 0.02	539.36 ± 7.30	13.05 ± 0.95
5h	26.15 ± 1.74	5.08 ± 0.33	523.45 ± 9.63	15.41 ± 0.04
5i	11.29 ± 0.98	1.12 ± 0.41	102.70 ± 5.26	9.22 ± 0.91
5j	34.06 ± 3.15	4.18 ± 0.27	116.15 ± 4.26	17.98 ± 0.30
5k	15.47 ± 1.06	2.42 ± 0.14	530.53 ± 6.04	16.72 ± 1.01
5l	27.14 ± 3.14	2.10 ± 0.10	133.10 ± 4.83	15.48 ± 0.06
5m	32.81 ± 2.18	5.45 ± 0.20	225.03 ± 5.86	12.07 ± 1.02
5n	17.12 ± 1.93	2.70 ± 0.08	265.52 ± 9.17	16.20 ± 0.07
5o	28.40 ± 2.37	7.22 ± 0.92	124.26 ± 8.20	15.64 ± 0.08
5p	12.63 ± 0.21	1.92 ± 0.08	541.39 ± 6.27	17.20 ± 0.08
Galantamine[a]	56.77 ± 1.26	14.20 ± 0.34	—	—
Clorgyline[b]	—	—	512.16 ± 11.34	—
EDT[c]	—	—	—	15.94 ± 0.62

[a] Reference inhibitor for acetylcholinesterase (AChE) and butyrylcholinesterase (BChE). [b] Reference inhibitor for monoamine oxidase-A (MAO-A). [c] Reference compound for metal chelating assay.

5d (IC_{50} = 15.31 ± 1.34 nM) were reported with moderate inhibitory properties.

Compounds **5i** (IC_{50} = 11.29 ± 0.98 nM) and **5p** (IC_{50} = 12.63 ± 0.21 nM) showed the strongest activity that is due to the strong EWG effect of the trifluoromethyl group and dichlorophenyl amino group, respectively. Compounds with electron-donating groups had a lower activity, such as **5e** (IC_{50} = 14.39 ± 2.07 nM) with *para*-methoxy phenyl group, **5g** (IC_{50} = 14.65 ± 1.03 nM) with naphthyl substitution, **5j** (IC_{50} = 34.06 ± 3.15 nM) with *o*-tolyl substitution and **5n** (IC_{50} = 17.12 ± 1.93 nM) with benzyl substitution.

Compounds with heterocyclic rings showed moderate activity due to the presence of electronegative hetero atoms in the rings and the electron-rich nature of these rings, such as **5d** (IC_{50} = 15.31 ± 1.34 nM) with thiophene substitution, **5h** (IC_{50} = 26.15 ± 1.74 nM) with pyridinyl substitution, **5k** (IC_{50} = 15.47 ± 1.06 nM) with 4-indole substitution and **5l** (IC_{50} = 27.14 ± 3.14 nM) with 3-indole substitution. Conversely, compound **5j** (IC_{50} = 34.06 ± 3.15 nM) with *ortho*-tolyl substitution displayed the lowest activity that can be explained by an electron-donating methyl group increasing the electron density of a phenyl ring and consequently reducing the inhibitory activity.

2.3.2 Butyrylcholinesterase (BChE). Enzyme butyrylcholinesterase (BChE) was tested and found to have an extremely high degree of inhibitory activity with IC_{50} values of 1.12 ± 0.41 nM to 8.24 ± 0.40 nM against the standard drug Galantamine (IC_{50} = 14.20 ± 0.34 nM). The most interesting compound is **5i** (IC_{50} = 1.12 ± 0.41 nM), where the phenyl ring is substituted by the 3-trifluoromethyl group having the strongest inhibitory effect and the lowest inhibition was that of **5f** (IC_{50} = 8.24 ± 0.40 nM) with the pyrazinyl group. Other electron-withdrawing groups such as fluorine and bromine with strong inhibitory activities were found in derivatives **5a** (IC_{50} = 1.64 ± 0.15 nM) and **5c** (IC_{50} = 4.17 ± 0.04 nM).

Heterocyclic derivatives such as **5b** (IC_{50} = 2.16 ± 0.26 nM) with pyridinyl, **5d** (IC_{50} = 4.62 ± 0.58 nM) with thiophene, **5k** (IC_{50} = 2.42 ± 0.14 nM) with 4-indole and **5l** (IC_{50} = 2.10 ± 0.10 nM) with 3-indole had moderate but significant inhibitory action. Compounds with electron-donating groups also have moderate inhibitory effects, such as **5e** (IC_{50} = 3.10 ± 0.17 nM) with methoxy on phenyl group substitution, **5m** (IC_{50} = 5.45 ± 0.20 nM) with furan substitution and **5n** (IC_{50} = 2.70 ± 0.08 nM) with benzyl substitution.

2.3.3 Monoamine oxidase A (MAO-A). The inhibitory effect against monoamine oxidase A of all the synthesized novel compounds was exceptionally good and it ranged between IC_{50} = 94.20 ± 5.57 nM and 551.53 ± 5.06 nM, confirming that compounds were dramatically more potent than the reference drug Clorgyline (IC_{50} = 512.16 ± 11.34 nM). Compound **5a** (IC_{50} = 94.20 ± 5.57 nM) had the strongest inhibitory effect due to strong EWG fluorine on the phenyl ring and compound **5f** (IC_{50} = 551.53 ± 5.06 nM) had the lowest inhibitory effect due to the pyrazine ring.

Heterocyclic compounds such as **5b** (IC_{50} = 423.01 ± 8.11 nM) with a pyridine ring, **5d** (IC_{50} = 504.76 ± 4.03 nM) with thiophene substitution, **5l** (IC_{50} = 133.10 ± 4.83 nM) with 3-indole substitution and **5m** (IC_{50} = 225.03 ± 5.86 nM) with a furan ring showed moderate inhibitory effects due to the electron-donating groups. Electron-donating groups such as **5e** (IC_{50} = 110.13 ± 7.21 nM) with methoxy on a phenyl group, **5g** (IC_{50} = 539.36 ± 7.30 nM) with a naphthyl group and **5n** (IC_{50} = 265.52 ± 9.17 nM) with benzyl group substitution also showed moderate inhibitory effect. Compounds **5f** (IC_{50} = 551.53 ± 5.06 nM) and **5p** (IC_{50} = 541.39 ± 6.27 nM) had the lowest inhibitory

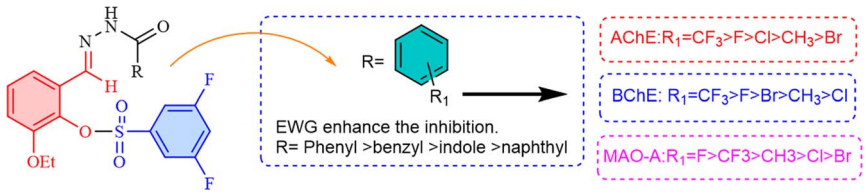

Scheme 2 Illustration of the SAR.

effect due to pyrazine and dichlorophenyl amino substitution (Scheme 2).

2.3.4 Antioxidant activity (metal chelating). All synthesized compounds **5(a–p)** were tested for their antioxidant potential in comparison with that of EDTA (IC_{50} = 15.94 ± 0.62 nM) as reference, and it ranged between IC_{50} = 9.22 ± 0.91 nM and 19.48 ± 0.05 nM. It means that some of the studied derivatives were found to be even more efficient antioxidants than the standard.

The strongest inhibition was revealed for compound **5i** (IC_{50} = 9.22 ± 0.91 nM) and the lowest for **5b** (IC_{50} = 19.48 ± 0.05 nM). Some compounds such as **5a** (IC_{50} = 11.27 ± 0.01 nM) that is a fluorine-based phenyl derivative, **5f** (IC_{50} = 14.50 ± 0.45 nM) that is a pyrazine-based derivative, **5g** (IC_{50} = 13.05 ± 0.95 nM) that is a naphthalene-based derivative, **5m** (IC_{50} = 12.07 ± 1.02 nM) that is a furan-based derivative have moderate inhibitory effects. Some other compounds such as **5e** (IC_{50} = 10.68 ± 0.07 nM), which is a methoxy phenyl derivative, and **5m** (IC_{50} = 12.07 ± 1.02 nM), which is a furan derivative, also have good inhibitory effects due to the strong electron-donating property.

Compounds with heterocyclic rings showed moderate inhibitory effects due to electronegative hetero atoms in the rings and the electron-rich nature of these rings, such as **5h** (IC_{50} = 15.41 ± 0.04 nM) with pyridinyl substitution, **5k** (IC_{50} = 16.72 ± 1.01 nM) with 4-indole substitution and **5l** (IC_{50} = 15.48 ± 0.06 nM) with 3-indole substitution. On the other hand, compound **5b** (IC_{50} = 19.48 ± 0.05 nM) with pyridine substitution displayed the lowest activity due to the electron-withdrawing nature of pyridine and electronegative nitrogen of pyridine pulling the electron density from the aromatic ring through the inductive and resonance effects.

2.4. Molecular docking and MM–GBSA analysis

In order to rationalize the experimentally observed multitarget inhibitory profile of the synthesized hydrazone derivatives **5(a–p)** against AChE, BChE and MAO-A, an integrated induced-fit docking (IFD) and MM–GBSA binding free energy approach was applied by means of the crystal structures of AChE (4EY7), BChE (6EQP) and MAO-A (2ZX5). IFD accounts for the flexibility of both ligands and active-site residues, consenting more realistic binding poses to be generated. The resulting complexes were then evaluated by MM–GBSA, which estimated the binding free energy by combining the molecular mechanics interaction energies with solvation effects, providing a quantitative measure of complex stability and enabling reliable correlation with the experimental IC_{50} values. The results are given in Table 2.

The IFD docking scores and MM–GBSA binding free energies provide a clear and highly consistent computational validation of the experimental multitarget inhibitory profile of compounds **5(a–p)** against MAO-A, AChE and BChE. For all three enzymes, every synthesized derivative exhibited substantially stronger binding than the corresponding reference drugs, confirming that the hydrazone scaffold was intrinsically well suited to these targets.

For MAO-A, all compounds showed IFD scores between −12.29 and −16.08 kcal mol^{-1}, which are dramatically better than that of clorgyline (−7.54 kcal mol^{-1}). Among them, **5p** (−16.076 kcal mol^{-1}) and **5i** (−15.740 kcal mol^{-1}) emerged as the strongest binders, and this trend was reinforced by their extremely favorable MM–GBSA energies of −119.84 and −108.98 kcal mol^{-1}, respectively. These values indicate exceptionally stable complexes and explain why halogen-rich derivatives such as **5p** (dichlorophenyl) and **5i** (CF_3-phenyl) display strong experimental MAO-A inhibition. In contrast, compounds such as **5k** and **5m**, although having favorable docking scores, had less favorable MMGBSA energies, indicating possible solvation or conformational strain, which is consistent with their reduced biological activity.

Table 2 IFD scores and MMGBSA Δ*G* binding energies of the synthesized compounds

	IFD docking scores (kcal mol^{-1})			MMGBSA Δ*G* binding energies (kcal mol^{-1})		
	2ZX5	4EY7	6EQP	2ZX5	4EY7	6EQP
Compound	MAO-A	AChE	BChE	MAO-A	AChE	BChE
5a	−13.732	−12.691	−9.774	−81.53	−75.57	−70.40
5b	−13.984	−12.767	−10.081	−67.35	−70.18	−58.36
5c	−14.365	−13.009	−11.671	−80.62	−69.39	−57.43
5d	−13.195	−11.359	−11.340	−67.04	−75.05	−68.74
5e	−13.192	−12.797	−10.791	−77.46	−81.29	−65.53
5f	−12.288	−12.159	−8.413	−78.21	−74.99	−61.29
5g	−13.687	−12.309	−8.809	−70.23	−78.74	−53.49
5h	−14.707	−11.997	−9.364	−81.82	−67.17	−56.95
5i	**−15.740**	**−13.607**	**−11.640**	**−108.98**	**−75.37**	**−75.92**
5j	−12.799	−12.168	−9.115	−67.97	−62.50	−57.77
5k	−15.617	−11.908	−10.942	−61.78	−72.66	−47.50
5l	−15.385	−12.497	−10.766	−79.46	−71.04	−62.17
5m	−12.467	−11.193	−8.192	−68.29	−57.51	−32.69
5n	−13.345	−11.962	−10.068	−86.68	−64.89	−45.14
5o	−13.124	−11.761	−10.337	−70.96	−80.27	−58.88
5p	−16.076	−12.016	−11.293	−119.84	−51.94	−76.78
Clorgyline	−7.543			−48.11		
Galantamine		−7.501	−5.407		−53.41	−31.65

In AChE, all derivatives again bound far more strongly than galantamine (−7.50 kcal mol^{-1}), with IFD scores ranging from −11.19 to −13.61 kcal mol^{-1}. Compound **5i** displayed the best docking score (−13.607 kcal mol^{-1}) and a very favorable ΔG binding energy (−75.37 kcal mol^{-1}), fully consistent with its lowest experimental IC_{50} value. **5e** also showed a particularly strong MM–GBSA energy (−81.29 kcal mol^{-1}), which explains its high AChE inhibitory potency despite not having the very

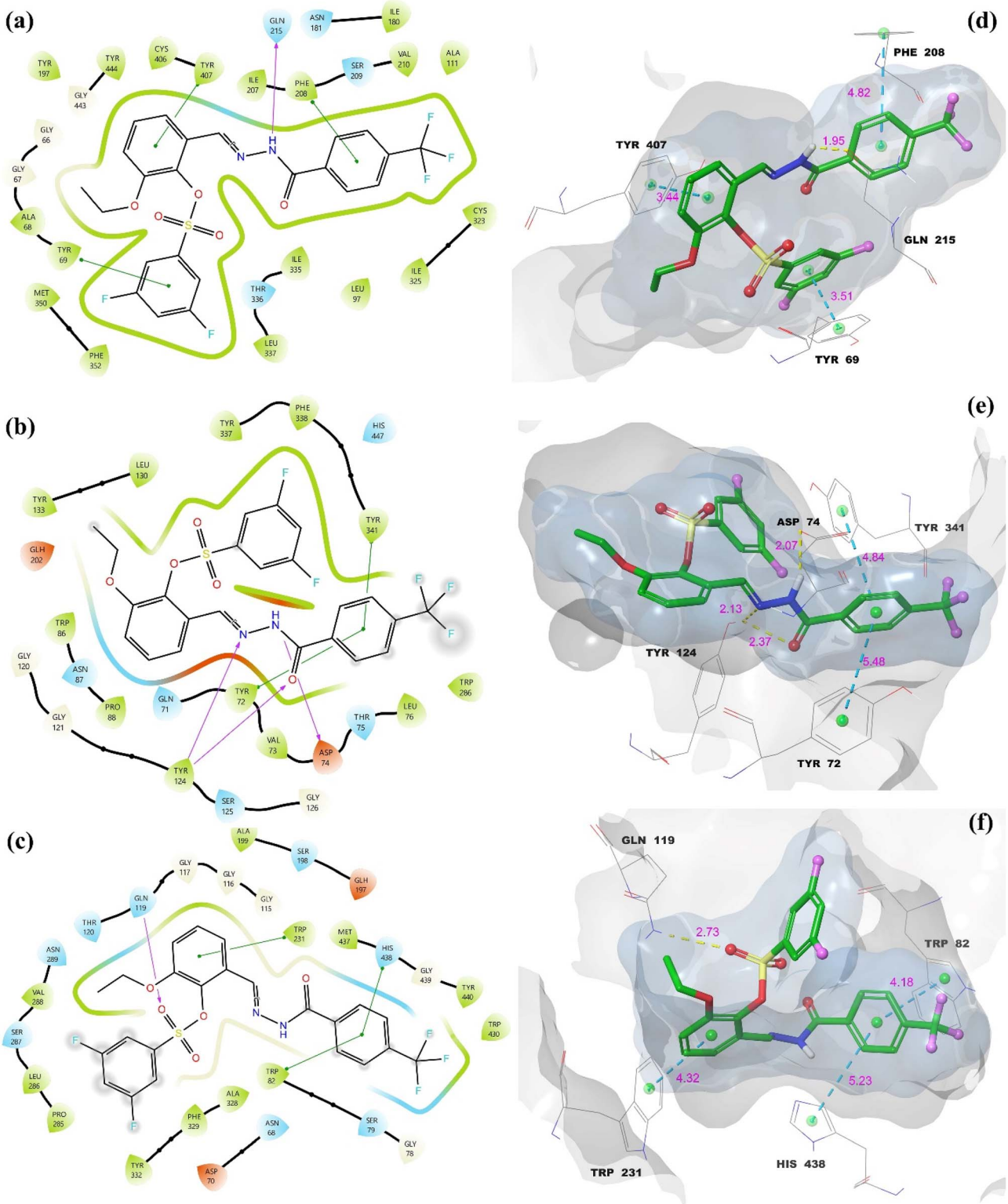

Fig. 2 Molecular docking of the 2D and 3D LPI between **5i** and MAOA, AChE and BChE: (a) 2D LPI of **5i**–**MAOA**, (b) 2D LPI of **5i**–**AChE**, (c) 2D LPI of **5i**–**BChE**, (d) 3D LPI of **5i**–**MAOA**, (e) 3D LPI of **5i**–**AChE** and (f) 3D LP of **5i**–**BChE**.

best docking score. The weaker ΔG bind of **5p** in AChE (-51.94 kcal mol^{-1}) explains why, despite excellent MAO-A and BChE binding, it is not the strongest AChE inhibitor experimentally.

For BChE (6EQP), the docking and MM–GBSA results highlight a strong preference for bulky, hydrophobic, and halogenated aromatic systems. **5i** (-75.92 kcal mol^{-1}) and **5p** (-76.78 kcal mol^{-1}) showed the most favorable MM–GBSA energies, consistent with their sub-nanomolar IC_{50} values, particularly the exceptional BChE inhibition of **5i** (1.12 nM). The larger active-site gorge of BChE accommodates these bulky CF_3- and dichlorophenyl-containing structures better than smaller or more polar heterocycles, which explains the much weaker binding of compounds such as **5m** (-32.69 kcal mol^{-1}) and **5n** (-45.14 kcal mol^{-1}).

In addition, the docking and MM–GBSA data strongly corroborate the experimental SAR. Electron-withdrawing and halogenated aromatic substituents, especially CF_3-phenyl (**5i**) and dichlorophenyl-amino (**5p**), maximize hydrophobic packing, π–π stacking, and electrostatic complementarity in the binding pockets of all three enzymes, producing the most stable complexes. Among all derivatives, **5i** stands out as the most balanced and potent multitarget lead, showing consistently strong docking scores and highly favorable binding free energies across MAO-A, AChE and BChE, in full agreement with its superior experimental inhibitory profile.

For visualizing the binding mode of the lead compound, 2D and 3D ligand–protein interaction poses of **5i** were evaluated for AChE, BChE and MAO-A, and they are given in Fig. 2. Fig. 2a represents the 2D ligand–protein interaction profile of compound **5i** within the MAO-A active site, where the hydrazide nitrogen forms a stabilizing hydrogen bond with Gln-215, anchoring the ligand in the catalytic cavity. In addition, three distinct π–π stacking interactions are observed in the aromatic-rich binding pocket: the difluorophenyl ring interacts with Tyr-69, the CF_3-substituted phenyl ring stacks with Phe-208, and the benzylidene aromatic ring engages in π–π stacking with Tyr-407, collectively enhancing hydrophobic packing and binding stability.

Fig. 2b represents the 2D LPI of compound **5i** with AChE, revealing an extensive interaction network involving both the catalytic active site (CAS) and the peripheral anionic site (PAS). The hydrazone carbonyl oxygen and hydrazone nitrogen form two separate hydrogen bonds with Tyr-124, while the remaining hydrazide nitrogen establishes an additional hydrogen bond with the PAS residue Asp-74. Moreover, the CF_3-phenyl ring participates in two π–π stacking interactions with Tyr-72 (PAS) and Tyr-341 (CAS), enabling simultaneous engagement of both binding regions.

Fig. 2c represents the 2D LPI of compound **5i** with BChE, where the sulfonyl group forms a hydrogen bond with Gln-119, contributing to proper ligand orientation within the active-site gorge. In parallel, the benzylidene aromatic ring shows a π–π stacking interaction with Trp-231, while the CF_3-phenyl ring engages in additional π–π stacking interactions with His-438 and Trp-82, highlighting the preference of BChE for bulky and hydrophobic aromatic substituents.

Fig. 2d–f represent the 3D ligand–protein interaction poses of compound **5i** within the active sites of MAO-A, AChE, and BChE, respectively. In all three complexes, yellow dashed lines denote hydrogen-bond interactions, whereas turquoise dashed lines indicate π–π stacking interactions. Across all the complexes, the hydrogen-bond distances range from 1.95 to 2.73 Å, while the π–π stacking interaction distances vary between 3.44 and 5.48 Å, confirming the formation of energetically favorable and geometrically optimal contacts.

In the 3D surface representations, the bluish cloud corresponds to the ligand surface binding area, while the gray cloud represents the protein surface binding region. A higher degree of surface overlap between these two regions reflects a better geometric fit of the ligand within the enzyme active site. In the MAO-A and AChE complexes, compound **5i** displays an almost complete surface complementarity, indicating tight accommodation within the catalytic cavities of both enzymes. In contrast, within the BChE complex, a slight solvent exposure of the difluorophenyl–sulfonyl moiety is observed, which can be attributed to the larger and more solvent-accessible active-site gorge of BChE. In summary, the 3D binding modes confirm the 2D interaction profile, where the hydrazone/hydrazide functional group is always the dominant hydrogen-bonding anchor. On the other hand, the aromatic rings and the CF_3-substituted phenyl moiety are responsible for the extensive π–π stacking and hydrophobic interactions in all three targets. This explains the balanced multitarget inhibitory profile of compound **5i** against MAO-A, AChE, and BChE.

2.5. Molecular dynamics simulations

For assessing the dynamic stability of the docked structures, 250 ns molecular dynamics simulations were performed for the **5i–MAO-A**, **5i–AChE**, and **5i–BChE** systems. The time-dependent stability of ligand binding was evaluated using root-mean-square deviation (RMSD) analyses, while root-mean-square fluctuation (RMSF) calculations were used to examine the residue-level flexibility and binding-site stability throughout the simulations.

MD simulation analysis of the **5i–MAO-A** complex is given in Fig. 3. Fig. 3a illustrates the key ligand–protein interactions maintained during the MD simulation, together with their percentage occupancies. The hydrazide nitrogen of compound **5i** forms a highly persistent hydrogen bond with Gln-215, which is preserved for 96% of the simulation time, indicating a strong anchoring interaction. In addition, the sulfonyl oxygen establishes a hydrogen bond with Lys-305 for approximately 40% of the trajectory. The difluorophenyl ring shows π–π stacking interactions for about 40%, while the benzylidene aromatic ring engages in π–π stacking with Tyr-407 and Tyr-444 for 71% and 44% of the simulation time, respectively.

Fig. 3b presents the RMSD profiles of the protein and ligand atoms throughout the 250 ns simulation. The RMSD of the protein Cα atoms reached a plateau at an average of about 1.75 Å, suggesting good equilibration of the protein structure. The RMSD of the ligand with respect to the protein (fit of ligand on protein) reached a stable value of about 2.4 Å, while the ligand

fit on ligand (ligand stability) was found to be highly stable with an average RMSD of about 0.9 Å.

The root-mean-square fluctuation (RMSF) analysis of protein atoms (Fig. 3c) reveals an average fluctuation of approximately 1.0 Å, with only a small degree of flexibility found at the ligand-binding and contact areas, as highlighted by the green markers of amino acid interactions. This finding suggests that ligand binding is a factor in the local protein environment's stabilization. At the same time, the ligand RMSF plot (Fig. 3d) reveals an average fluctuation of only 1.25 Å, confirming the conformational stability of compound **5i** in the MAO-A active site.

Fig. 3e shows the fractional interaction histogram, which summarizes the cumulative interaction behaviors over the course of the simulation. This analysis reflects both simultaneous interactions of a given ligand with multiple residues and

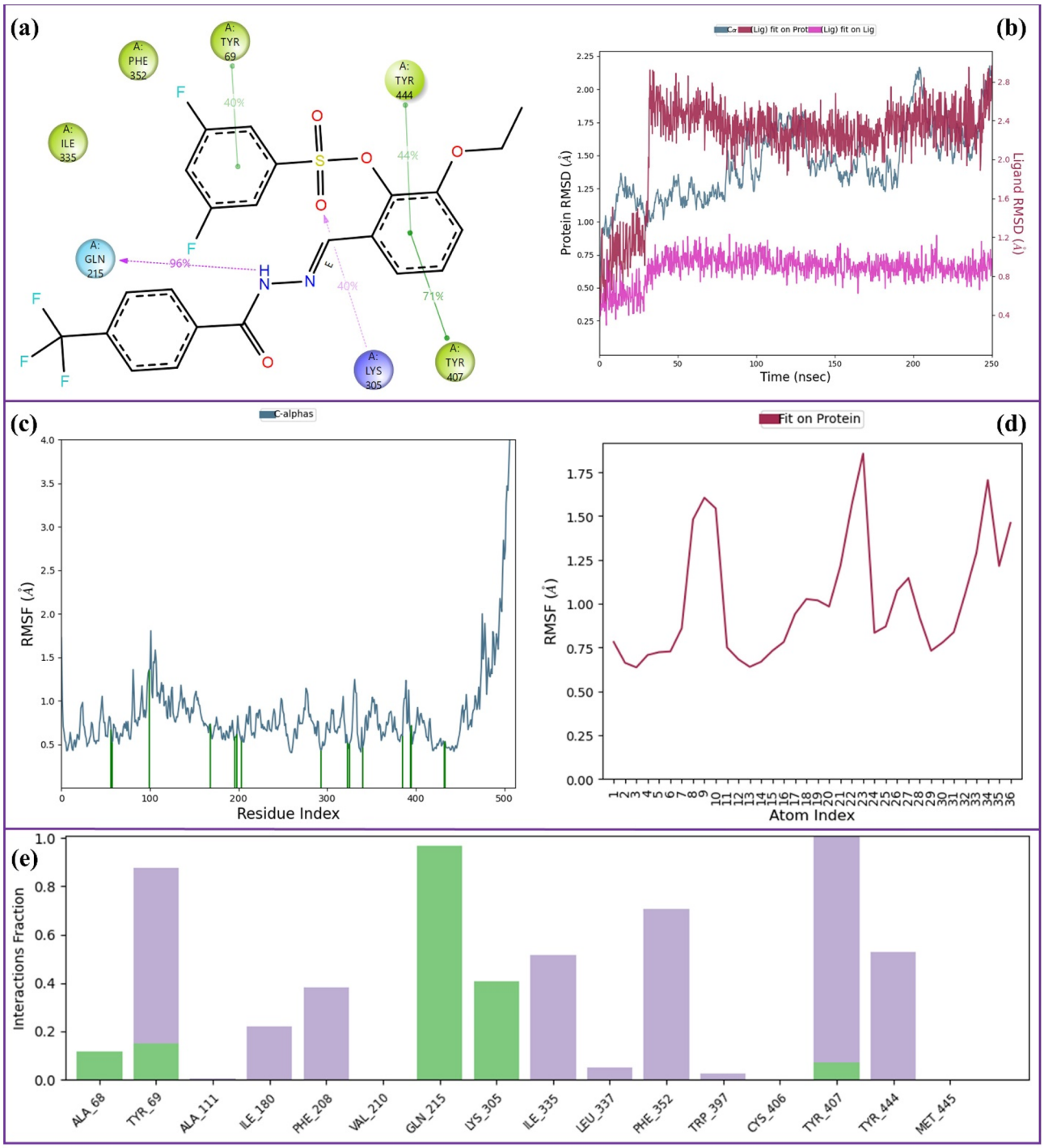

Fig. 3 MD simulation analysis of the **5i–MAO-A** complex: (a) 2D key LPI with the percentage simulation period, (b) RMSD of the protein and ligand atoms, (c) RMSF of the protein atoms, (d) RMSF of the ligand atoms and (e) fractional interaction histogram during the simulation time.

situations in which individual residues interact with different ligand groups. In the histogram, green bars represent hydrogen bonds, purple bars indicate hydrophobic interactions, and blue bars indicate water-mediated hydrogen bonds. The residues that most frequently participate in interactions are Gln-215, Tyr-407, Tyr-69, Phe-352, and Tyr-444, highlighting their key roles in the stabilization of the **5i–MAO-A** complex during the MD simulation.

MD simulation analysis of the **5i–AChE** complex is given in Fig. 4. Fig. 4a illustrates the key ligand–protein interactions of compound **5i** with AChE maintained during the MD simulation together with their percentage occupancies. The hydrazide nitrogen forms a hydrogen bond with Asp-74 for 52% of the simulation time, while the hydrazide carbonyl oxygen establishes a highly persistent hydrogen bond with Tyr-124, which is maintained for 86% of the trajectory. In addition, the CF_3-

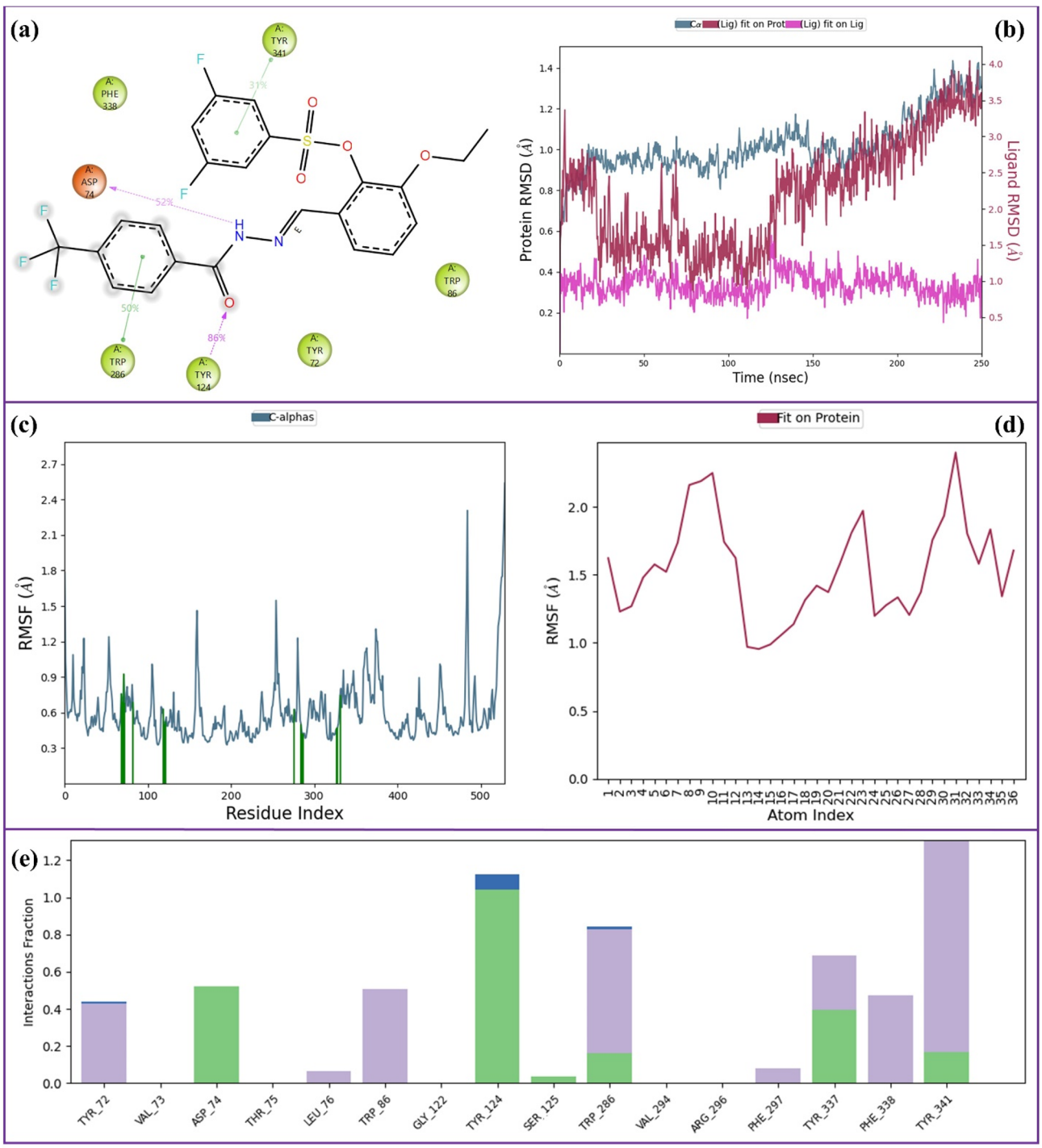

Fig. 4 MD simulation analysis of the **5i–AChE** complex: (a) 2D key LPI with the percentage simulation period, (b) RMSD of the protein and ligand atoms, (c) RMSF of the protein atoms, (d) RMSF of the ligand atoms and (e) fractional interaction histogram during the simulation time.

substituted phenyl ring engages in a π–π stacking interaction with Trp-286 for 50% of the simulation period, whereas the difluorophenyl ring shows π–π stacking with Tyr-241 for 31%, supporting stable aromatic interactions within both the catalytic and peripheral regions of AChE.

The RMSD profiles presented in Fig. 4b demonstrate that the protein backbone remains stable throughout the 250 ns simulation, with an average Cα RMSD of approximately 1.2 Å. The ligand RMSD relative to the protein (ligand fit on protein) stabilizes around 2.5 Å, while the internal conformational stability of the ligand (ligand fit on ligand) remains high, with an average RMSD of 1.0 Å.

As shown in Fig. 4c, the root-mean-square fluctuation (RMSF) calculation for protein atoms shows an average fluctuation of about 1.0 Å, which represents a lack of flexibility for the binding-site residues. As expected, the ligand RMSF plot in

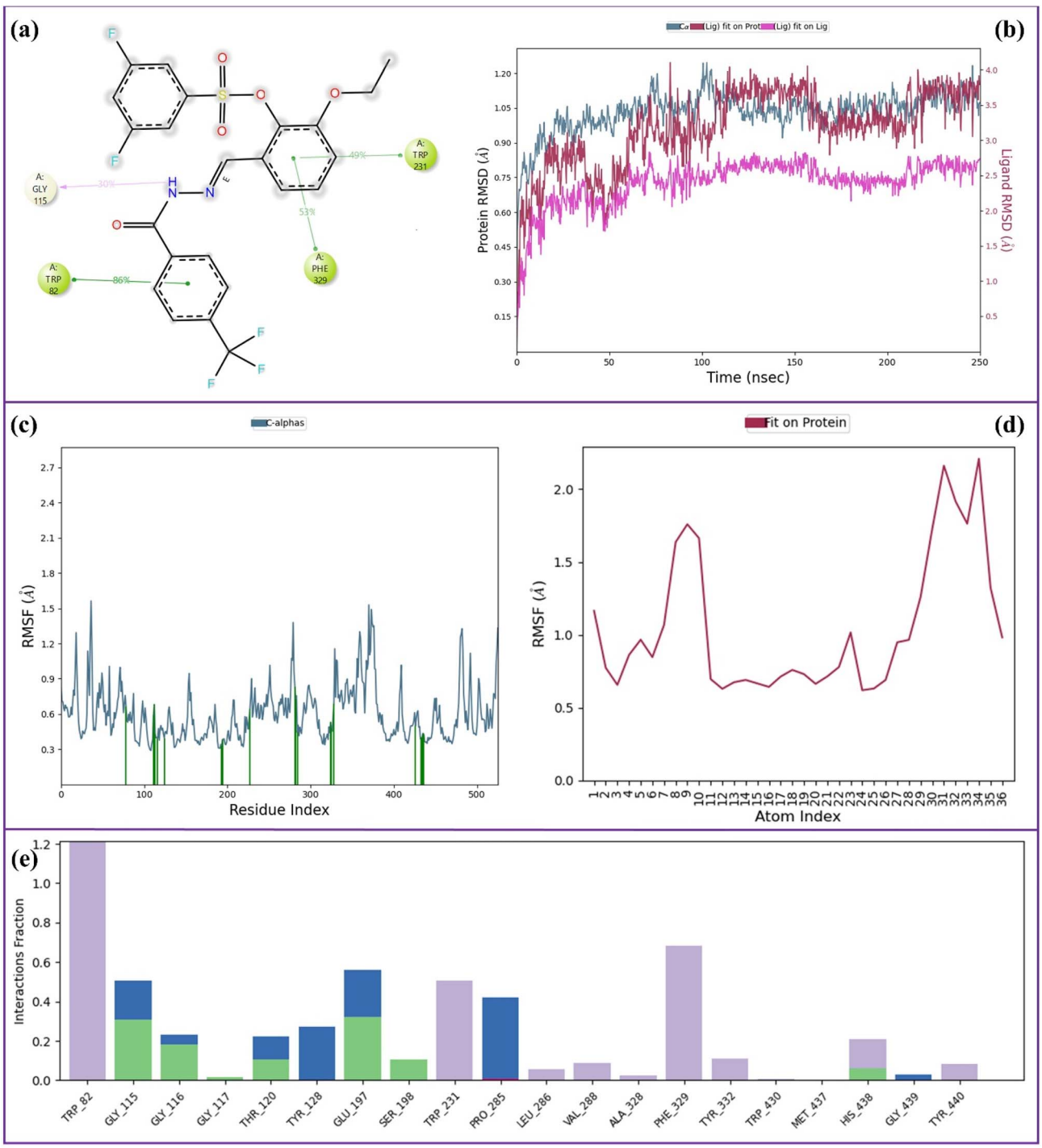

Fig. 5 MD simulation analysis of the **5i–BChE** complex: (a) 2D key LPI with the percentage simulation period, (b) RMSD of the protein and ligand atoms, (c) RMSF of the protein atoms, (d) RMSF of the ligand atoms and (e) fractional interaction histogram during the simulation time.

Fig. 4d shows an average fluctuation of about 1.75 Å, which further supports the fact that compound **5i** maintains a stable binding pose in the acetylcholinesterase (AChE) active site. The fractional interaction histogram shown in Fig. 4e is a representation of the cumulative interaction behavior. The most frequently interacting residues include Tyr-341, Tyr-124, and Trp-286, highlighting their central roles in stabilizing the **5i–AChE** complex over the course of the MD trajectory.

MD simulation analysis of the **5i–BChE** complex is given in Fig. 5. Fig. 5a illustrates the key ligand–protein interactions of compound **5i** with BChE during the MD simulation. The hydrazide nitrogen forms a hydrogen bond with Gly-115 for 30% of the trajectory, while the CF_3-substituted phenyl ring shows a highly persistent π–π stacking interaction with Trp-82 (86%). Additional π–π stacking interactions are observed between the benzylidene ring and Phe-329 (53%) and Trp-231 (49%), emphasizing the role of aromatic interactions in complex stabilization. The RMSD analysis (Fig. 5b) indicates a stable protein backbone with an average Cα RMSD of 1.1 Å. Although the ligand shows a higher RMSD relative to the protein (3.5 Å), consistent with the flexible BChE active-site gorge, its internal conformation remains stable (2.5 Å). The RMSF plot reveals small oscillations for both the protein (approximately 1.0 Å) and the ligand (roughly 1.5 Å) in Fig. 5c and d. In the analysis of the fractional interaction histogram (Fig. 5e), Trp-82 emerges as the prominent interacting residue, followed by Phe-329, Glu-197, Trp-231, and Pro-285. These residues, in combination, contribute to the stabilization of the **5i–BChE** complex.

Comparative 250 ns MD simulations indicate that the **5i–MAO-A** complex is the most dynamically stable, followed by **5i–AChE**, while **5i–BChE** shows higher ligand mobility, consistent with its larger active-site gorge. This trend is supported by RMSD and RMSF analyses, which reveal lower ligand fluctuations in MAO-A and AChE, and increased flexibility in the BChE complex. Residue interaction analysis identifies Gln-215 (MAO-A) and Tyr-124 (AChE) as dominant hydrogen-bond anchors, whereas Trp-82 plays a key stabilizing role in BChE through persistent π–π stacking. Across all systems, the hydrazide/hydrazone moiety serves as the main hydrogen-bonding element, while the aromatic rings contribute to stability *via* π–π and hydrophobic interactions.

2.6. Geometry optimization and frontier molecular orbitals

The optimized structures and frontier molecular orbitals (FMOs) of the four *in vitro* most active compounds (**5a**, **5d**, **5i**,

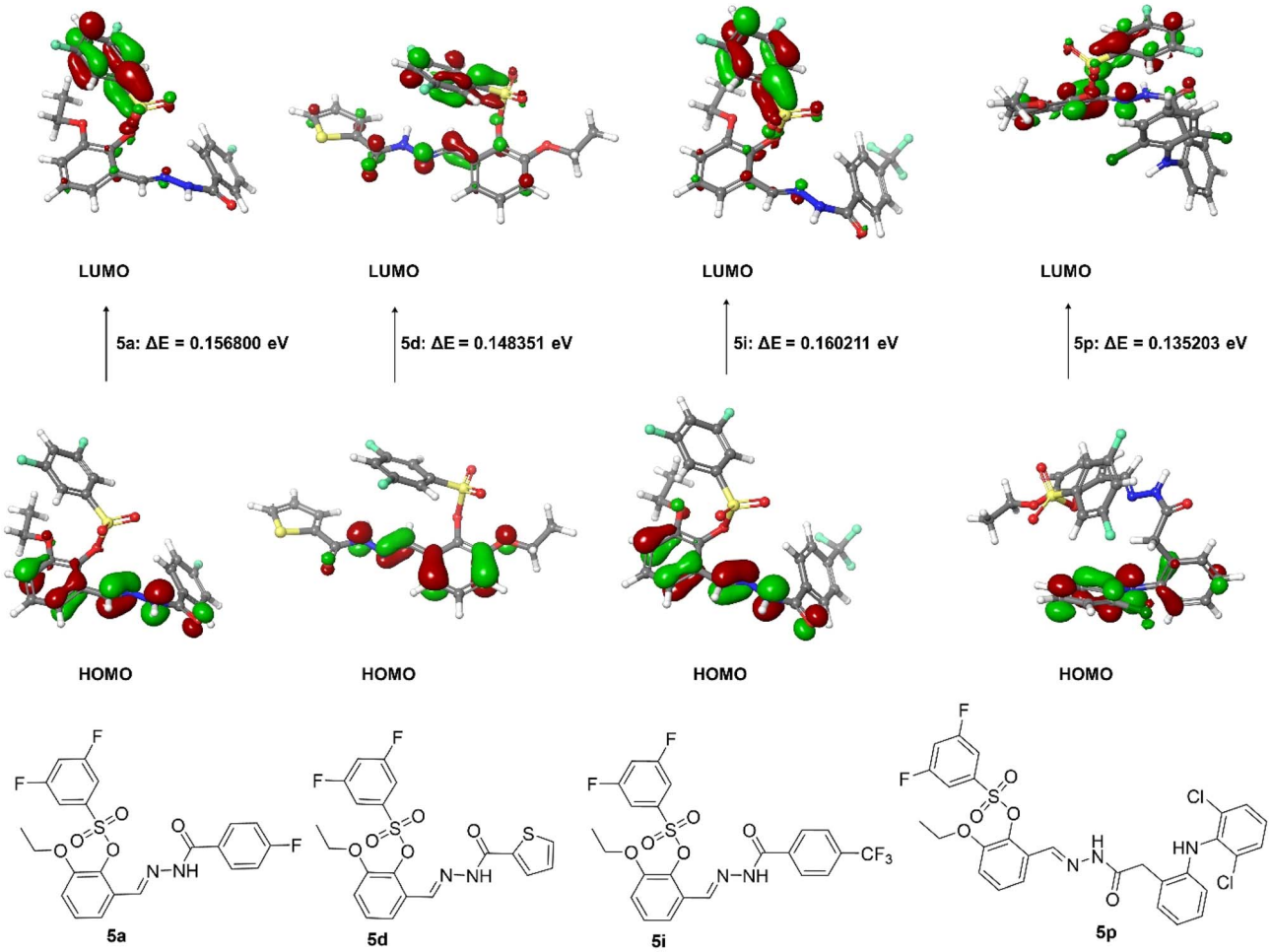

Fig. 6 HOMO–LUMO energy gaps of the selected compounds.

Table 3 HOMO–LUMO energies of the selected compounds

Compound	HOMO (eV)	LUMO (eV)	ΔE (eV)
5a	−0.240028	−0.083228	0.156800
5d	−0.235767	−0.087416	0.148351
5i	−0.245113	−0.084902	0.160211
5p	−0.213401	−0.078198	0.135203

Table 4 Electrostatic potential for the selected compounds

Compound	ESP neg. mean (eV^2)	ESP pos. mean (eV^2)
5a	0.281	0.355
5d	0.309	0.296
5i	0.255	0.366
5p	0.222	0.213

and **5p**) were calculated using density functional theory with the B3LYP functional and the 6-311G++** basis set. As shown in Fig. 6 and Table 3, all tested compounds had negative HOMO and LUMO energy levels, suggesting that they are thermodynamically stable and have a good ability to participate in electronic interactions. The HOMO–LUMO distributions also suggested that the biological activities of the compounds are closely related to their electronic structures.

The HOMO–LUMO energy values for the chosen compounds (Table 3) demonstrate a distinct difference in the electronic nature and reactivity among the compounds. Among these compounds, **5p** has the lowest energy gap (ΔE = 0.135 eV), which suggests higher chemical reactivity, higher polarizability, and higher ability to participate in charge transfer interactions. Conversely, compound **5i** has the highest HOMO–LUMO energy gap (ΔE = 0.160 eV), suggesting relatively high electronic stability and low reactivity.

Compounds **5a** and **5d** have intermediate ΔE values of 0.157 and 0.148 eV, respectively, which indicate a relatively balanced electronic nature between stability and reactivity. Notably, the lower HOMO energy value of **5i** (−0.245 eV) suggests a lower ability to donate electrons, whereas the higher HOMO energy level of **5p** (−0.213 eV) suggests its higher ability to donate electrons. These findings collectively suggest that compound **5p** is the most electronically reactive compound, while compound **5i** is the most electronically stable among the chosen compounds.

2.7. Electrostatic potential analysis

Molecular electrostatic potential (MEP) maps show the distribution of electron density and the areas where electrophilic or nucleophilic attack is possible. The negative areas (red) indicate electron-rich, nucleophilic regions, while the positive areas (blue) represent electrophilic regions. As seen in Fig. 7, compounds **5a**, **5d**, **5i**, and **5p** have different electrostatic potential maps. Compound **5d** has the most negative potential, indicating its higher nucleophilicity, while compound **5i** has relatively high positive areas, as expected for its higher electrophilicity. Compounds **5a** and **5p** have relatively balanced electrostatic properties.

The qualitative results are always supported by the quantitative data shown in Table 4. Compound **5d** has the highest mean negative electrostatic potential (ESP) value (0.309 eV^2), suggesting a higher electron-rich property and a higher affinity for nucleophilic interactions. On the other hand, compound **5i** has the highest mean positive ESP value (0.366 eV^2), suggesting a higher affinity for electrophilic interactions. Compound **5a** has a balanced distribution of negative and positive ESP values, while compound **5p** has the lowest ESP values in general, suggesting a more evenly distributed electrostatic potential with less polarization of the electrostatic surface.

2.8. Global chemical reactivity descriptors

The Global Chemical Reactivity (GCR) parameters, including electronegativity (χ), chemical potential (μ), hardness (η), softness (S), and electrophilicity (ω), provide information on the reactivity, stability, and bioactivity of molecules. The GCR parameters are useful for predicting interactions with enzymes or receptors, which can be applied in drug design. The GCR

Table 5 GCR descriptors of the selected compounds

Compound	ΔE (eV)[a]	μ (eV)[b]	η (eV)[c]	S (eV^{-1})[d]	χ (eV)[e]	ω (eV)[f]
5a	0.156800	−0.16163	0.07840	6.377	0.16163	0.167
5d	0.148351	−0.16159	0.07418	6.738	0.16159	0.176
5i	0.160211	−0.16501	0.08011	6.241	0.16501	0.170
5p	0.135203	−0.14580	0.06760	7.395	0.14580	0.157

GCR descriptors: [a] energy gap (ΔE) = $E_{LUMO} - E_{HOMO}$; [b] chemical potential (μ) = ($E_{HOMO} + E_{LUMO}$)/2; [c] global hardness (η) = ($E_{LUMO} - E_{HOMO}$)/2; [d] global softness (S) = 1/2 × η; [e] electronegativity (χ) = −1/2 × ($E_{HOMO} + E_{LUMO}$); and [f] global electrophilicity index (ω) = $\mu^2/2\eta$.

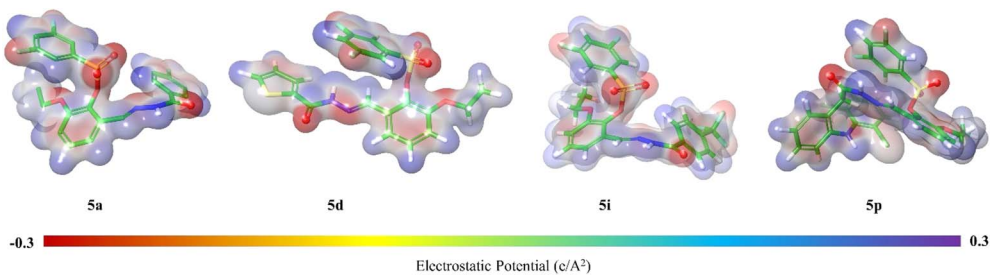

Fig. 7 Molecular electrostatic potential for the selected compounds.

Table 6 IC_{50} (μM) values of the compounds **5a–p** in HUVEC cells (MTT assay, mean ± SD, and $n = 3$)

Compound	IC_{50} [μM] HUVEC
5a	43.81 ± 1.85
5b	38.74 ± 1.92
5c	61.25 ± 2.88
5d	36.58 ± 1.67
5e	57.42 ± 2.61
5f	49.36 ± 2.14
5g	41.27 ± 1.98
5h	63.18 ± 2.95
5i	58.72 ± 2.65
5j	35.94 ± 1.73
5k	52.83 ± 2.47
5l	60.11 ± 2.79
5m	47.65 ± 2.20
5n	64.27 ± 2.98
5o	39.85 ± 1.89
5p	49.18 ± 2.89

parameters of the chosen chromone-hydrazone compounds are shown in Table 5.

The descriptors of GCR for compounds **5a**, **5d**, **5i**, and **5p** are summarized in Table 4, focusing on the differences in their electronic reactivity. Compound **5i** has the highest HOMO–LUMO gap ($\Delta E = 0.1602$ eV) and hardness ($\eta = 0.0801$ eV), while compound **5p** has the lowest ΔE (0.1352 eV), lowest hardness, and highest softness ($S = 7.395$ eV^{-1}), which indicate higher reactivity and polarizability. The compound with the most negative chemical potential and highest electronegativity is **5i**, while the highest electrophilicity index ($\omega = 0.176$ eV) is found in **5d**, which indicates higher electron-accepting ability. Based on these results, compound **5i** is the most stable, compound **5p** is the most reactive, and compound **5d** is the most electrophilic among the four compounds.

2.9. Cytotoxicity assays

To evaluate the preliminary safety profile of the synthesized compounds, cytotoxicity studies were carried out on HUVEC (ATCC® CRL-1730™) cells using the MTT assay. The compounds (**5a–p**) were tested at different concentrations (200–1 μM) to assess their effects on cell viability. The results of the cytotoxicity assays are presented in Table 6.

Cytotoxicity results (Table 6) revealed that all compounds showed moderate effects on HUVEC cells, with IC_{50} values ranging between 35.94 and 64.27 μM. Importantly, the most active compounds in enzyme inhibition and docking studies (*e.g.*, **5i** and **5p**) exhibited relatively low cytotoxicity ($IC_{50} > 49$ μM). These findings indicate that the compounds possess a favorable safety profile and a reasonable therapeutic window.

3. Conclusion

In conclusion, the hydrazones of 2-ethoxy-6-formylphenyl 3,5-difluorobenzenesulfonate were successfully synthesized, and their *in silico* and molecular docking analyses showed great promise as anti-AChE, anti-BChE, and MAO-A inhibitors. The synthesized new compounds demonstrated inhibitory activity: $IC_{50} = 1.12 \pm 0.41$ nM to 8.24 ± 0.40 nM for BChE, $IC_{50} = 94.20 \pm 5.57$ nM to 551.53 ± 5.06 nM for MOA-A and $IC_{50} = 9.22 \pm 0.91$ nM to 19.48 ± 0.05 nM for antioxidant activities. Notably, compound **5i** exhibited the highest inhibitory activity with $IC_{50} = 11.29 \pm 0.98$ nM for AChE, $IC_{50} = 1.12 \pm 0.41$ nM for BChE, $IC_{50} = 102.70 \pm 5.26$ nM for MOA-A and $IC_{50} = 9.22 \pm 0.91$ nM for metal chelating activity against the reference drug Galantamine $IC_{50} = 56.77 \pm 1.26$ nM for AChE, $IC_{50} = 14.20 \pm 0.34$ nM for BChE, reference drug Clorgyline $IC_{50} = 512.16 \pm 11.34$ nM for MOA-A and EDTA $IC_{50} = 15.94 \pm 0.62$ nM as reference for antioxidant metal chelating activity. Molecular docking studies also support these findings, showing strong binding to the key residues in the catalytic pockets of AChE, BChE, and MAO-A. Additionally, ADME analysis shows acceptable pharmacokinetic profiles, which supports the drug-likeness and potential development of these compounds. Antioxidant analysis also shows that these compounds have the capacity to scavenge free radicals and protect against oxidative stress, suggesting a complementary role in neuroprotection alongside the inhibition of enzymes. The compounds exhibited moderate cytotoxicity in HUVEC cells, with IC_{50} values ranging from 35.94 to 64.27 μM, indicating a favorable safety profile within the tested concentration range. Overall, this finding offers a strong basis for the design and optimization of multi-target compounds that combine cholinesterase and MAO-A inhibition with antioxidant properties. Such properties are highly relevant for the advance of next-generation therapeutics for complex neurodegenerative pathways. Further structural refinement and biological evaluation are recommended to advance these promising candidates towards clinical applications.

4. Experimental

4.1. Chemistry

The reagents used for the synthesis of 2-ethoxy-6-formylphenyl 3,5-difluorobenzenesulfonate-based hydrazones (**5**) were purchased from Sigma-Aldrich. Solvents and reagents, such as ethanol, methanol, glacial acetic acid, petroleum ether, ethyl acetate, triethylamine and dimethylformamide, were purchased from Merck and used without further purification. The reaction progress was monitored by thin-layer chromatography using silica gel plates. ^{1}H NMR and ^{13}C NMR spectra were recorded using a Bruker Ascend 400 MHz NMR spectrometer in deuterated solvents and DMSO-d_6 (400–500 MHz and 101–126 MHz frequencies), respectively, at 25 °C. These are provided against the chemical shift (ppm) and coupling constant (J) in Hertz (Hz) and the signal multiplicities are indicated as singlet, doublet, multiplet and so on.

4.2. Synthesis of 2-ethoxy-6-formylphenyl 3,5-difluorobenzenesulfonate (3)

The synthesis of the compound 2-ethoxy-6-formylphenyl 3,5-difluorobenzenesulfonate (**3**) was performed by the method reported earlier:[47] in brief, 3-ethoxysalicylaldehyde (**1**) (7 mmol) was dissolved in 5 ml of DMF and triethylamine (7 mmol) was

added to a round-bottom flask. Low temperature was maintained in an ice bath by stirring the reaction mixture. After that, 3,5-difluorobenzene-1-sulfonyl chloride (**2**) (7 mmol) was added dropwise over a period one hour. The mixture was gently stirred, and the reaction progress was monitored using thin-layer chromatography (TLC). An aliquot volume of the reaction mixture (60 min) was neutralized with the addition of 20 ml cold distilled water, and the product precipitated. The precipitate was dried, filtered and stored.

4.3. General method for the synthesis and characterization of compounds 5(a–p)

The equimolar quantities (0.26 mmol) of various substituted hydrazides **4(a–p)** were reacted with 2-ethoxy-6-formylphenyl 3,5-difluorobenzenesulfonate (**3**) in 10 ml of methanol, in the presence of glacial acetic acid (catalytic amount) to obtain hydrazones **5(a–p)**. The heated reaction mix was refluxed overnight at 65–70 °C. Thin-layer chromatography (TLC) was performed to track the process of reactions. Once it was complete, the mixture was cooled to room temperature, resulting in solid products that were filtered and washed repeatedly using methanol before drying at room temperature. The products obtained were the target hydrazones **5(a–p)**.

4.3.1 (*E*)-2-Ethoxy-6-[(2-(4-fluorobenzoyl)hydrazineylidene) methyl]phenyl-3,5-difluorobenzenesulfonate (5a). Off-white powder; m.p.: 162–164 °C; yield = 75%, δ_H (500 MHz, DMSO-d_6) 12.10 (1H, s), 8.57 (1H, s), 8.08–7.92 (2H, m), 7.85 (1H, t, J = 9.0 Hz), 7.68 (2H, d, J = 3.8 Hz), 7.57 (1H, d, J = 7.7 Hz), 7.39 (3H, q, J = 7.6 Hz, 7.0 Hz), 7.19 (1H, d, J = 8.0 Hz), 3.88 (2H, q, J = 6.9 Hz), 1.06 (3H, t, J = 6.9 Hz). ^{13}C NMR (126 MHz, DMSO-d_6) δ 165.72, 163.77, 163.67, 162.66, 161.76, 161.66, 151.57, 142.18, 139.02, 138.95, 138.87, 137.16, 130.96, 130.89, 130.19, 130.07, 129.02, 118.05, 116.06, 115.89, 115.70, 112.82, 112.76, 112.65, 112.59, 111.43, 111.23, 111.02, 64.70, 14.40; ESI-HRMS *m*/*z*: chemical formula: $C_{22}H_{17}F_3N_2O_5S$, calculated $[M + H]^+$ = 479.08885, found $[M + H]^+$ = 479.08706.

4.3.2 (*E*)-2-Ethoxy-6-[(2-picolinoylhydrazineylidene)methyl] phenyl-3,5-difluorobenzenesulfonate (5b). Light brown solid; m.p.: 124–126 °C; yield = 75%, δ_H (500 MHz, DMSO-d_6) 12.42 (1H, s), 8.82–8.70 (2H, m), 8.14 (1H, d, J = 7.8 Hz), 8.07 (1H, m), 7.85–7.75 (1H, m), 7.75–7.62 (3H, m), 7.57 (1H, d, J = 7.4 Hz), 7.38 (1H, t, J = 8.1 Hz), 7.20 (1H, d, J = 8.1 Hz), 3.88 (2H, q, J = 6.9 Hz), 1.08 (3H, t, J = 6.9 Hz). ^{13}C NMR (126 MHz, DMSO-d_6) δ 163.73, 163.63, 161.72, 161.62, 161.20, 151.63, 149.96, 148.99, 143.79, 138.93, 138.46, 137.17, 130.33, 129.00, 127.55, 123.28, 118.18, 115.76, 112.84, 112.77, 112.67, 112.60, 111.41, 111.21, 111.00, 64.73, 14.45; ESI-HRMS *m*/*z*: chemical formula: $C_{21}H_{17}F_2N_3O_5S$, calculated $[M + H]^+$ = 462.09352, found $[M + H]^+$ = 462.09205.

4.3.3 (*E*)-2-[(2-(4-Bromobenzoyl)hydrazineylidene)methyl]-6-ethoxyphenyl-3,5-difluorobenzenesulfonate (5c). Light yellow solid; m.p.: 172–174 °C; yield = 69%, δ_H (400 MHz, DMSO-d_6) 12.14 (1H, s), 8.58 (1H, s), 7.86 (3H, t, J = 11.5 Hz), 7.78 (3H, d, J = 8.1 Hz), 7.67 (2H, d, J = 4.1 Hz), 7.57 (1H, d, J = 7.8 Hz), 7.39 (1H, t, J = 8.0 Hz), 7.20 (1H, d, J = 8.1 Hz), 3.88 (3H, q, J = 7.0 Hz), 1.06 (4H, t, J = 7.0 Hz). ^{13}C NMR (101 MHz, DMSO-d_6) δ 164.03, 163.90, 162.77, 161.52, 161.40, 151.57, 142.44, 139.03, 138.94, 138.84, 137.18, 132.67, 132.01, 130.26, 130.14, 129.45, 129.03, 128.39, 126.20, 120.44, 120.07, 118.06, 115.76, 113.00, 112.85, 112.64, 112.55, 111.49, 111.23, 110.98, 64.71, 14.40; ESI-HRMS *m*/*z*: chemical formula: $C_{22}H_{17}{}^{79}BrF_2N_2O_5S$, calculated $[M + H]^+$ = 539.00879, found $[M + H]^+$ = 539.00748; chemical formula: $C_{22}H_{17}{}^{81}BrF_2N_2O_5S$, calculated $[M + H]^+$ = 541.00670, found $[M + H]^+$ = 541.00529.

4.3.4 (*E*)-2-Ethoxy-6-((2-(thiophene-2-carbonyl) hydrazineylidene)methyl)phenyl-3,5-difluoro benzenesulfonate (5d). White powder; m.p.: 204–206 °C; yield = 83%, δ_H (400 MHz, DMSO-d_6) 12.05 (1H, d, J = 29.3 Hz), 8.36 (1H, d, J = 137.1 Hz), 8.11–7.88 (2H, m), 7.84 (1H, t, J = 9.1 Hz), 7.68 (3H, d, J = 4.1 Hz), 7.41 (1H, s), 7.32–7.14 (2H, m), 3.89 (2H, s), 1.08 (3H, s). ^{13}C NMR (101 MHz, DMSO-d_6) δ 164.04, 163.91, 161.53, 161.41, 138.87, 137.15, 135.52, 129.10, 118.08, 115.67, 112.83, 112.54, 111.25, 111.00, 64.75, 14.42; ESI-HRMS *m*/*z*: chemical formula: $C_{20}H_{16}F_2N_2O_5S_2$, calculated $[M + H]^+$ = 467.05470, found $[M + H]^+$ = 467.05352.

4.3.5 (*E*)-2-Ethoxy-6-((2-(2-methoxybenzoyl) hydrazineylidene)methyl)phenyl-3,5-difluorobenzene sulfonate (5e). White shiny crystals; m.p.: 164–166 °C; yield = 91%, δ_H (400 MHz, DMSO-d_6) 11.74 (1H, s), 8.42 (1H, s), 7.89–7.80 (1H, m), 7.67 (2H, t, J = 6.0 Hz), 7.60–7.48 (3H, m), 7.38 (1H, t, J = 8.1 Hz), 7.22–7.14 (2H, m), 7.07 (1H, t, J = 7.4 Hz), 3.93–3.82 (6H, m), 1.07 (3H, t, J = 6.9 Hz). ^{13}C NMR (101 MHz, DMSO-d_6) δ 164.00, 163.88, 163.23, 161.50, 161.37, 157.11, 151.59, 141.50, 138.99, 137.12, 132.56, 130.20, 130.08, 128.97, 124.22, 120.89, 118.03, 115.63, 112.79, 112.70, 112.59, 112.50, 112.35, 111.21, 64.71, 56.24, 14.42; ESI-HRMS *m*/*z*: chemical formula: $C_{23}H_{20}F_2N_2O_6S$, calculated $[M + H]^+$ = 491.10884, found $[M + H]^+$ = 491.10749.

4.3.6 (*E*)-2-Ethoxy-6-((2-(pyrazine-2-carbonyl) hydrazineylidene)methyl)phenyl-3,5-difluorobenzenesulfonate (5f). Shiny yellow powder; m.p.: 192–194 °C; yield = 90%, δ_H (400 MHz, DMSO-d_6) 12.57 (1H, s), 9.28 (1H, d, J = 1.4 Hz), 8.95 (1H, d, J = 2.5 Hz), 8.82 (1H, dd, J = 2.3 Hz, 1.5 Hz), 8.76 (1H, s), 7.81 (1H, m), 7.66 (2H, d, J = 4.2 Hz), 7.57 (1H, dd, J = 7.9 Hz, 1.2 Hz), 7.40 (1H, t, J = 8.1 Hz), 7.21 (1H, d, J = 7.6 Hz), 3.88 (2H, q, J = 6.9 Hz), 1.08 (3H, t, J = 7.0 Hz). ^{13}C NMR (101 MHz, DMSO-d_6) δ 164.00, 163.87, 161.49, 161.37, 160.29, 151.62, 148.38, 145.05, 144.68, 144.46, 143.83, 138.97, 138.88, 137.24, 130.12, 129.06, 118.21, 115.99, 112.86, 112.78, 112.67, 112.57, 111.24, 110.99, 64.74, 14.44; ESI-HRMS *m*/*z*: chemical formula: $C_{20}H_{16}F_2N_4O_5S$, calculated $[M + H]^+$ = 463.08877, found $[M + H]^+$ = 463.08717.

4.3.7 (*E*)-2-((2-(2-Naphthoyl)hydrazineylidene)methyl)-6-ethoxyphenyl-3,5-difluorobenzenesulfonate (5g). White powder; m.p.: 132–134 °C; yield = 99%, δ_H (400 MHz, DMSO-d_6) 12.27 (1H, s), 8.49 (1H, s), 8.27–8.19 (1H, m), 8.12 (1H, d, J = 8.3 Hz), 8.08–8.00 (1H, m), 7.87 (1H, m), 7.75 (1H, dd, J = 7.1 Hz, 1.3 Hz), 7.69–7.60 (6H, m), 7.41 (1H, t, J = 8.1 Hz), 7.21 (1H, dd, J = 8.3 Hz, 1.4 Hz), 3.88 (2H, q, J = 7.0 Hz), 1.05 (4H, t, J = 7.0 Hz). ^{13}C NMR (101 MHz, DMSO-d_6) δ 164.78, 163.52, 163.40, 161.01, 160.89, 151.08, 141.56, 138.50, 136.71, 133.14, 132.46, 130.63, 129.90, 129.64, 128.54, 128.36, 128.25, 127.13, 126.66, 126.45, 126.06, 125.94, 125.03, 124.93, 117.53, 115.28, 112.32, 112.23, 112.12, 112.03, 111.00, 110.74, 110.48, 64.20, 13.89; ESI-HRMS

m/*z*: chemical formula: $C_{26}H_{20}F_2N_2O_5S$, calculated $[M + H]^+$ = 511.11392, found $[M + H]^+$ = 511.11276.

4.3.8 (*E*)-2-Ethoxy-6-((2-isonicotinoylhydrazineylidene) methyl)phenyl-3,5-difluorobenzenesulfonate (5h). White powder; m.p.: 127–129 °C; yield = 83%, δ_H (500 MHz, DMSO-d_6) 12.30 (1H, s), 8.82 (2H, s), 8.59 (1H, s), 7.92–7.79 (3H, m), 7.67 (2H, m), 7.58 (1H, dd, J = 8.0 Hz, 1.4 Hz), 7.40 (1H, t, J = 8.1 Hz), 7.22 (1H, dd, J = 8.4 Hz, 1.5 Hz), 3.88 (2H, q, J = 7.0 Hz), 1.06 (3H, t, J = 6.9 Hz). ^{13}C NMR (126 MHz, DMSO-d_6) δ 163.77, 163.67, 162.29, 161.77, 161.67, 151.58, 150.84, 150.05, 143.34, 140.67, 138.88, 138.80, 137.25, 129.93, 129.10, 122.03, 118.12, 116.01, 112.85, 112.79, 112.68, 112.62, 111.47, 111.27, 111.07, 64.73, 14.40; ESI-HRMS *m*/*z*: chemical formula: $C_{21}H_{17}F_2N_3O_5S$, calculated $[M + H]^+$ = 462.09352, found $[M + H]^+$ = 462.09182.

4.3.9 (*E*)-2-Ethoxy-6-((2-(4-(trifluoromethyl)benzoyl) hydrazineylidene)methyl)phenyl-3,5-difluorobenzenesulfonate (5i). Brown powder; m.p.: 148–150 °C; yield = 75%, δ_H (500 MHz, DMSO-d_6) 12.28 (1H, s), 8.59 (1H, s), 8.12 (2H, d, J = 7.9 Hz), 7.95 (2H, d, J = 8.1 Hz), 7.86 (2H, t, J = 9.1 Hz), 7.68 (2H, d, J = 5.1 Hz), 7.58 (1H, d, J = 7.9 Hz), 7.40 (1H, t, J = 8.1 Hz), 7.21 (1H, d, J = 8.2 Hz), 3.88 (2H, q, J = 7.0 Hz), 1.06 (3H, t, J = 7.0 Hz). ^{13}C NMR (126 MHz, DMSO) δ 163.78, 163.68, 162.61, 161.77, 161.67, 151.58, 142.93, 138.92, 137.42, 137.23, 130.04, 129.12, 129.06, 125.99, 125.96, 125.94, 118.10, 115.88, 112.83, 112.77, 112.66, 112.60, 111.46, 111.25, 64.72, 14.39; ESI-HRMS *m*/*z*: chemical formula: $C_{23}H_{17}F_5N_2O_5S$, calculated $[M + H]^+$ = 529.08566, found $[M + H]^+$ = 529.08406.

4.3.10 (*E*)-2-Ethoxy-6-((2-(2-methylbenzoyl) hydrazineylidene)methyl)phenyl-3,5-difluorobenzenesulfonate (5j). White powder; m.p.: 148–150 °C; yield = 88%, δ_H (500 MHz, DMSO-d_6) 12.01 (1H, s), 8.43 (1H, s), 7.94–7.85 (1H, m), 7.67 (3H, td, J = 6.0 Hz, 2.4 Hz), 7.59 (1H, dd, J = 8.0 Hz, 1.4 Hz), 7.47–7.27 (6H, m), 7.20 (1H, dd, J = 8.3 Hz, 1.4 Hz), 3.88 (3H, q, J = 7.0 Hz), 2.39 (3H, s), 1.06 (4H, t, J = 6.9 Hz). ^{13}C NMR (126 MHz, DMSO-d_6) δ 165.77, 163.76, 163.66, 161.75, 161.66, 151.58, 141.63, 139.01, 137.18, 136.44, 135.46, 131.10, 130.52, 130.12, 128.98, 128.91, 127.93, 127.78, 126.11, 125.60, 117.94, 115.69, 112.77, 112.71, 112.60, 112.54, 111.45, 111.25, 111.04, 64.70, 19.76, 14.41; ESI-HRMS *m*/*z*: chemical formula: $C_{23}H_{20}F_2N_2O_5S$, calculated $[M + H]^+$ = 475.11392, found $[M + H]^+$ = 475.11241.

4.3.11 (*E*)-2-((2-(1*H*-Indole-4-carbonyl)hydrazineylidene) methyl)-6-ethoxyphenyl-3,5-difluorobenzenesulfonate (5k). Light brown solid; m.p.: 222–224 °C; yield = 85%, δ_H (500 MHz, DMSO-d_6) 12.01 (1H, s), 11.39 (1H, s), 8.55 (1H, s), 7.86 (1H, m), 7.73–7.66 (2H, m), 7.62 (2H, dd, J = 14.8 Hz, 7.6 Hz), 7.56–7.46 (2H, m), 7.39 (1H, t, J = 8.0 Hz), 7.27–7.14 (2H, m), 6.86 (1H, s), 3.88 (2H, q, J = 6.9 Hz), 1.07 (4H, t, J = 7.0 Hz). ^{13}C NMR (126 MHz, DMSO-d_6) δ 164.96, 163.76, 163.66, 161.75, 161.65, 151.58, 141.06, 139.12, 139.04, 138.97, 137.10, 136.99, 130.49, 128.94, 127.41, 126.82, 125.22, 120.57, 119.46, 117.97, 115.41, 112.81, 112.74, 112.64, 112.57, 111.41, 111.21, 111.01, 102.15, 64.69, 14.43; ESI-HRMS *m*/*z*: chemical formula: $C_{24}H_{19}F_2N_3O_5S$, calculated $[M + H]^+$ = 500.10917, found $[M + H]^+$ = 500.10719.

4.3.12 (*E*)-2-((2-(1*H*-Indole-3-carbonyl)hydrazineylidene) methyl)-6-ethoxyphenyl-3,5-difluorobenzenesulfonate (5l). White shiny solid; m.p.: 212–214 °C; yield = 90%, δ_H (500 MHz, DMSO-d_6) 11.80 (1H, s), 11.61 (1H, s), 8.41 (1H, s), 8.33–8.16 (2H, m), 7.83 (1H, m), 7.75–7.64 (2H, m), 7.56 (1H, d, J = 7.9 Hz), 7.50 (1H, m), 7.38 (1H, t, J = 8.1 Hz), 7.25–7.13 (3H, m), 3.89 (2H, q, J = 6.9 Hz), 1.08 (3H, t, J = 6.9 Hz). ^{13}C NMR (126 MHz, DMSO-d_6) δ 163.77, 163.67, 161.76, 161.66, 151.63, 139.11, 139.03, 138.96, 136.92, 130.69, 128.94, 122.78, 121.63, 121.31, 117.90, 115.05, 112.79, 112.73, 112.62, 112.56, 112.46, 111.39, 111.18, 110.98, 64.68, 14.43; ESI-HRMS *m*/*z*: chemical formula: $C_{24}H_{19}F_2N_3O_5S$, calculated $[M + H]^+$ = 500.10917, found $[M + H]^+$ = 500.10758.

4.3.13 (*E*)-2-Ethoxy-6-((2-(furan-2-carbonyl) hydrazineylidene)methyl)phenyl-3,5-difluorobenzenesulfonate (5m). Off-white powder; m.p.: 168–170 °C; yield = 77%, δ_H (500 MHz, DMSO-d_6) 12.09 (1H, s), 8.56 (1H, s), 8.01–7.94 (1H, m), 7.83 (1H, m), 7.72–7.60 (2H, m), 7.54 (1H, d, J = 7.9 Hz), 7.39 (1H, d, J = 8.1 Hz), 7.33 (1H, s), 7.19 (1H, dd, J = 8.2 Hz, 1.5 Hz), 6.73 (1H, dd, J = 3.5 Hz, 1.7 Hz), 3.87 (2H, q, J = 6.9 Hz), 1.06 (4H, t, J = 6.9 Hz). ^{13}C NMR (126 MHz, DMSO-d_6) δ 163.76, 163.66, 161.75, 161.65, 154.75, 151.57, 146.87, 146.57, 142.15, 138.91, 138.84, 137.10, 130.17, 129.04, 118.05, 115.68, 112.82, 112.76, 112.65, 112.59, 111.44, 111.23, 111.03, 64.71, 14.42; ESI-HRMS *m*/*z*: chemical formula: $C_{20}H_{16}F_2N_2O_6S$, calculated $[M + H]^+$ = 451.07754, found $[M + H]^+$ = 451.07594.

4.3.14 (*E*)-2-Ethoxy-6-((2-(2-phenylacetyl)hydrazineylidene) methyl)phenyl-3,5-difluorobenzenesulfonate (5n). Light green powder; m.p.: 160–162 °C; yield = 85%, δ_H (400 MHz, DMSO-d_6) 11.71 (1H, d, J = 108.6 Hz), 8.21 (1H, d, J = 103.3 Hz), 7.84 (1H, dd, J = 9.3 Hz, 2.2 Hz), 7.72–7.64 (2H, m), 7.56–7.45 (1H, m), 7.37–7.30 (5H, m), 3.87 (2H, dd, J = 11.3 Hz, 7.0 Hz), 1.10–1.01 (3H, m). ^{13}C NMR (101 MHz, DMSO-d_6) δ 172.42, 166.73, 163.53, 163.41, 161.02, 160.90, 156.69, 151.14, 150.98, 140.27, 138.51, 136.96, 136.47, 135.54, 135.43, 129.59, 129.36, 129.07, 128.71, 128.51, 128.47, 128.33, 128.27, 128.20, 126.61, 126.38, 118.40, 117.42, 117.38, 115.07, 114.87, 112.34, 112.26, 112.05, 111.97, 110.98, 110.73, 110.47, 64.23, 64.17, 13.91, 13.87; ESI-HRMS *m*/*z*: chemical formula: $C_{23}H_{20}F_2N_2O_5S$, calculated $[M + H]^+$ = 475.11392, found $[M + H]^+$ = 475.11245.

4.3.15 (*E*)-2-((2-(2-Chlorobenzoyl)hydrazineylidene) methyl)-6-ethoxyphenyl-3,5-difluorobenzenesulfonate (5o). Brown hard solid, m.p.: 153–155 °C; yield = 78%, δ_H (500 MHz, DMSO-d_6) 12.19 (1H, s), 8.28 (1H, d, J = 143.1 Hz), 7.93–7.84 (1H, m), 7.67 (2H, m), 7.61–7.57 (2H, m), 7.55 (1H, m), 7.51–7.36 (2H, m), 7.20 (1H, dd, J = 8.3 Hz, 1.1 Hz), 7.01 (1H, m), 3.94–3.74 (2H, m), 1.05 (3H, m). ^{13}C NMR (126 MHz, DMSO-d_6) δ 169.30, 163.75, 163.65, 163.09, 161.74, 161.64, 151.58, 151.54, 142.30, 138.97, 138.59, 137.22, 137.05, 136.21, 135.48, 131.99, 131.16, 130.85, 130.26, 130.22, 129.91, 129.82, 129.75, 129.42, 129.22, 129.04, 128.92, 127.76, 127.41, 117.95, 117.24, 115.89, 115.49, 112.77, 112.73, 112.71, 112.67, 112.60, 112.54, 112.50, 111.33, 111.27, 64.70, 14.38; ESI-HRMS *m*/*z*: chemical formula: $C_{22}H_{17}ClF_2N_2O_5S$, calculated $[M + H]^+$ = 495.05930, found $[M + H]^+$ = 495.05760.

4.3.16 (*E*)-2-((2-(2-(2-((2,6-Dichlorophenyl)amino)phenyl) acetyl)hydrazineylidene)methyl)-6-ethoxyphenyl 3,5-difluorobenzenesulfonate (5p). White powder, m.p.: 196–194 °C; yield = 78%, δ_H (500 MHz, DMSO-d_6) 11.94 (1H, d, J = 127.9 Hz), 8.27 (1H, d, J = 117.4 Hz), 7.84 (1H, m), 7.73–7.65 (2H, m), 7.65–7.59 (1H, m), 7.56–7.49 (2H, m), 7.36 (1H, m), 7.27 (1H, m), 7.22–7.14 (2H, m), 7.08 (1H, m), 6.89 (1H, m), 6.32 (1H, m), 4.14 (1H,

s), 3.87 (2H, m), 3.73 (1H, s), 1.05 (3H, m). ^{13}C NMR (126 MHz, DMSO-d_6) δ 173.65, 168.53, 163.77, 163.67, 161.76, 161.66, 161.65, 151.65, 151.47, 143.62, 143.40, 141.78, 139.07, 138.99, 138.92, 138.49, 137.53, 137.15, 137.01, 131.47, 131.00, 130.50, 130.06, 129.95, 129.91, 129.69, 129.64, 129.02, 128.03, 127.84, 126.01, 125.75, 125.03, 124.58, 121.38, 121.15, 118.05, 118.01, 116.62, 116.24, 115.80, 115.57, 112.78, 112.74, 112.68, 112.61, 112.55, 112.50, 111.27, 111.24, 64.74, 64.69, 38.69, 36.05, 14.41, 14.36; ESI-HRMS *m*/*z*: chemical formula: $C_{29}H_{23}Cl_2F_2N_3O_5S$, calculated $[M + H]^+ = 634.07818$, found $[M + H]^+ = 634.07606$.

4.4. Computational studies

All molecular docking, molecular dynamics (MD), and density functional theory (DFT) calculations were carried out using the Schrödinger Maestro suite.

Molecular docking studies were conducted using Glide implemented in Maestro (version 14.3), while MD simulations were performed with Desmond integrated into Maestro (version 13.9), following computational protocols used in our previous studies. The crystal structures of MAO-A (PDB ID: 2Z5X), AChE (PDB ID: 4EY7), and BChE (PDB ID: 6EQP) were retrieved from the Protein Data Bank and prepared using the Protein Preparation Wizard, including bond order assignment, optimization of protonation and ionization states, addition of missing hydrogen atoms, and removal of crystallographic water molecules not involved in ligand binding. The docking grids were placed around the active sites, which were defined by the co-crystallized ligands. Extra Precision (XP) docking was used to predict the binding modes of compound **5i** to the active sites of the target enzymes. To further consider the flexibility of the receptors and improve the ligand–protein interactions, Induced Fit Docking (IFD) was carried out, producing a maximum of 20 poses for each ligand. The most preferred binding poses were chosen based on the docking scores and interaction patterns. The binding free energies of the complexes were then calculated using the prime MM–GBSA method with the VSGB model, which allowed flexibility of the active-site residues while constraining the rest of the protein.[48–50]

To evaluate the dynamic stability of the docked complexes, 250 ns molecular dynamics (MD) simulations were carried out for the **5i–MAO-A**, **5i–AChE**, and **5i–BChE** complexes in NPT ensemble simulations (300 K and 1 atm). The complexes were solvated in explicit TIP4P water, neutralized, and added with 0.15 M NaCl to simulate physiological conditions. Energy minimization and MD simulations were performed using the OPLS4e force field. Trajectory analyses included calculations of RMSD and RMSF values, as well as evaluations of hydrogen bonds, hydrophobic interactions, π–π stacking, water-mediated bridges, and ionic interactions, providing a comprehensive assessment of the stability and conformational behavior of the ligand–enzyme complexes over time.[51–54]

Concurrently, density functional theory (DFT) studies were carried out to investigate the electronic properties and reactivity of the most active compounds (**5a**, **5d**, **5i**, and **5p**). All quantum chemical calculations were carried out using the Jaguar module of Schrödinger Maestro (version 14.3). Geometry optimizations and frontier molecular orbital (FMO) analyses were carried out using the B3LYP functional with the 6-31G++** basis set without imposing any symmetry constraints. The properties module was used to calculate the essential electronic parameters, such as HOMO–LUMO energy levels, energy gaps, molecular electrostatic potential (MEP), electrostatic potential (ESP), and global conceptual reactivity (GCR) parameters. For the specific investigation of surface charge distribution and electrostatic interaction patterns, the Atomic Electrostatic Potential (AEP) option was used. All optimized structures were confirmed to be true energy minima by the absence of imaginary frequencies. The calculated electronic parameters were used to assess the stability, charge transfer ability, and interaction potential of the compounds, which justified their observed biological activities.[55,56]

4.5. Enzyme inhibition and antioxidant studies

4.5.1 AChE and BChE assays. AChE and BChE inhibitory activities of the test compounds were determined by a slightly modified colorimetric Ellman assay.[57,58] In these experiments, AChE from *Electrophorus electricus* (electric eel) and BChE from horse serum were used as enzyme sources. Acetylthiocholine iodide (AChI) and butyrylthiocholine iodide (BChI) served as the corresponding substrates, whereas 5,5′-dithiobis(2-nitrobenzoic acid) (DTNB) was used as the chromogenic reagent. For the assay, the reaction medium contained a Tris–HCl buffer (1.0 M, pH 8.0), a test compound solution of different concentrations, and deionized water. Then, the enzyme solution was added to the mixture and pre-incubated at 25 °C for 10 min to allow interaction between the enzyme and the inhibitor candidate. After this incubation period, a DTNB solution (0.5 mM) was introduced. The enzymatic reaction was initiated by adding AChI or BChI as substrates. During the reaction, enzymatic hydrolysis of AChI or BChI generated thiocholine, which subsequently reacted with DTNB to produce the yellow-colored 5-thio-2-nitrobenzoate (TNB) anion. The formation of TNB was monitored spectrophotometrically at 412 nm, and the change in absorbance was used to evaluate the enzyme activity.[59,60] A control experiment without any inhibitor and a suitable blank were included under the same experimental conditions. The IC_{50} values were obtained from the plots of inhibition percentage *versus* compound concentration using nonlinear regression analysis.

4.5.2 MAO-A assay. Monoamine oxidase-A (MAO-A) inhibitory activity was evaluated using recombinant human MAO-A enzyme (Sigma-Aldrich or equivalent commercial source). The assay was carried out in a potassium phosphate buffer (50 mM, pH 7.4), which was used for the preparation of all solutions. The enzyme solution was freshly prepared in the same buffer prior to use.[61] The test compounds were dissolved in dimethyl sulfoxide (DMSO) and diluted with buffer to obtain the desired concentrations, ensuring that the final DMSO content did not exceed 1% (v/v). In a typical assay, the buffer, test compound, and MAO-A enzyme solution were mixed and pre-incubated at 37 °C for 10 min. The reaction was initiated by adding an appropriate substrate such as kynuramine. Following enzymatic oxidation, kynuramine is converted into 4-hydroxyquinoline, and the formation of this fluorescent product was measured

spectrofluorometrically (excitation at 310 nm and emission at 380 nm). Control experiments without inhibitor and blank samples were included under identical conditions.[62] The percentage inhibition was calculated by comparing the enzymatic activity in the presence and absence of test compounds, and the IC_{50} values were determined from the dose–response curves. All experiments were conducted in triplicate ($n = 3$), and the results are expressed as mean ± standard deviation.

4.5.3 Metal chelating assay. The ferrous ion chelating capacity of the test compounds was determined according to a colorimetric method based on the disruption of the Fe^{2+}–ferrozine complex.[63] Briefly, different concentrations of the test compounds were prepared in an appropriate solvent. An aliquot of each sample solution was mixed with an $FeCl_2$ solution (2 mM), and the mixture was allowed to stand briefly at room temperature. Subsequently, a ferrozine solution (5 mM) was added to initiate the complex formation. After incubation for 10 min at room temperature, the absorbance was measured at 562 nm using a UV-Vis spectrophotometer. A control containing all reagents except the test compound was prepared under the same conditions, while EDTA was used as the reference chelating agent.[64] The decrease in absorbance indicated the chelation of ferrous ions by the tested compounds, which interfered with the formation of the Fe^{2+}–ferrozine complex. The metal chelating activity was calculated as percentage inhibition using the following equation: chelating activity (%) $= [(A_0 - A_1)/A_0] \times 100$, where A_0 is the absorbance of the control and A_1 is the absorbance in the presence of the sample. IC_{50} values, defined as the concentration of the compound required to chelate 50% of ferrous ions, were determined from the plots of chelating activity (%) *versus* compound concentration.[65] All experiments were conducted in triplicate, and the results are expressed as mean ± standard deviation.

4.6. Cytotoxicity studies

The cytotoxic effects of compounds **5a–p** were evaluated in HUVEC (Human Umbilical Vein Endothelial Cells, ATCC® CRL-1730™) using the MTT assay. The cells were cultured in DMEM supplemented with 10% fetal bovine serum (FBS) and 1% penicillin–streptomycin under standard conditions (37 °C, 5% CO_2, humidified atmosphere).[66]

For the assay, HUVEC cells were seeded into 96-well plates and allowed to attach for 24 h. Subsequently, cells were treated with compounds **5a–p** at eight different concentrations (200–1 μM, serially diluted). After 24 h incubation, the MTT solution was added to each well and incubated for an additional 3–4 h. The resulting formazan crystals were dissolved in DMSO, and the absorbance was measured at 570 nm using a microplate reader. The cell viability was expressed as a percentage relative to the untreated control cells.[67,68]

Author contributions

Arooj Fatima and Faiqa Noreen: investigation and formal analysis. Parham Taslimi: biological activity, formal analysis, and data curation. Halil Şenol and Mostafa A. Ismail: investigation, formal analysis, data curation, software, and resources. Rima D. Alharthy and Asif Rasool: formal analysis and validation. Magdi E. A. Zaki and Sobhi M. Gomha: data curation, resources, and funding acquisition. Zahid Shafiq: writing – original draft, supervision, and conceptualization.

Conflicts of interest

The authors declare that they have no known competing financial interests or personal relationships that could have appeared to influence the work reported in this paper.

Data availability

All data generated or analyzed during this study are included in this published article and its supplementary information (SI) files. Supplementary information: ^{1}HNMR, ^{13}CNMR and HRMS spectra. See DOI: https://doi.org/10.1039/d6ra01071g.

Acknowledgements

The authors extend their appreciation to the Deanship of Research and Graduate Studies at King Khalid University, Saudi Arabia, through Large Research Project under grant number for the year 1447.

References

1 E. Bozkurt, *et al.*, Design and bioevaluation of novel hydrazide-hydrazones derived from 4-acetyl-N-substituted benzenesulfonamide, *Russ. J. Bioorg. Chem.*, 2020, **46**, 702–714.
2 X. Zhao, *et al.*, Dual-Target Inhibitors Based on Acetylcholinesterase: Novel Agents for Alzheimer's Disease, *Eur. J. Med. Chem.*, 2024, 116810.
3 B. S. K. Aktar, Design, Synthesis, Anticholinesterase and Antidiabetic Inhibitory Activities, and Molecular Docking of Novel Fluorinated Sulfonyl Hydrazones, *ACS Omega*, 2024, **9**(40), 42037.
4 S. Hameed, *et al.*, Evaluation of synthetic 2-aryl quinoxaline derivatives as α-amylase, α-glucosidase, acetylcholinesterase, and butyrylcholinesterase inhibitors, *Int. J. Biol. Macromol.*, 2022, **211**, 653–668.
5 R. Kandimalla, V. Thirumala and P. H. Reddy, Is Alzheimer's disease a type 3 diabetes? A critical appraisal, *Biochim. Biophys. Acta, Mol. Basis Dis.*, 2017, **1863**(5), 1078–1089.
6 Y. Yang and W. Song, Molecular links between Alzheimer's disease and diabetes mellitus, *Neuroscience*, 2013, **250**, 140–150.
7 F. Rahim, *et al.*, Synthesis and in vitro acetylcholinesterase and butyrylcholinesterase inhibitory potential of hydrazide based Schiff bases, *Bioorg. Chem.*, 2016, **68**, 30–40.
8 M. Bajda, *et al.*, Structure-based search for new inhibitors of cholinesterases, *Int. J. Mol. Sci.*, 2013, **14**(3), 5608–5632.
9 M. S. Benedetti, Biotransformation of xenobiotics by amine oxidases, *Fundam. Clin. Pharmacol.*, 2001, **15**(2), 75–84.

10 A. T. Gulledge and G. J. Stuart, Cholinergic inhibition of neocortical pyramidal neurons, *J. Neurosci.*, 2005, **25**(44), 10308–10320.
11 S. Khan, *et al.*, Design, synthesis, in vitro biological assessment and in silico molecular modeling study of thiazole-thiazolidinone derivatives as potent anti-cancer agents, *Results Chem.*, 2024, **7**, 101507.
12 B. Evranos-Aksöz, *et al.*, Synthesis and screening of human monoamine oxidase-A inhibitor effect of new 2-pyrazoline and hydrazone derivatives, *Arch. Pharm.*, 2015, **348**(10), 743–756.
13 A. D. Bokare and W. Choi, Review of iron-free Fenton-like systems for activating H2O2 in advanced oxidation processes, *J. Hazard. Mater.*, 2014, **275**, 121–135.
14 E. Başaran, *et al.*, Design, synthesis, and in silico and in vitro cytotoxic activities of novel isoniazid–hydrazone analogues linked to fluorinated sulfonate esters, *ACS Omega*, 2024, **9**(15), 17551–17562.
15 D. Osmaniye, *et al.*, Design, synthesis, in vitro and in silico studies of some novel triazoles as anticancer agents for breast cancer, *J. Mol. Struct.*, 2021, **1246**, 131198.
16 A. Singh, *et al.*, Oxidative stress: a key modulator in neurodegenerative diseases, *Molecules*, 2019, **24**(8), 1583.
17 R. Thanan, *et al.*, Oxidative stress and its significant roles in neurodegenerative diseases and cancer, *Int. J. Mol. Sci.*, 2014, **16**(1), 193–217.
18 M. Duhan, *et al.*, Quantitative structure activity relationship studies of novel hydrazone derivatives as α-amylase inhibitors with index of ideality of correlation, *J. Biomol. Struct. Dyn.*, 2022, **40**(11), 4933–4953.
19 Ł. Popiołek, *et al.*, New hydrazide–hydrazones of isonicotinic acid: Synthesis, lipophilicity and in vitro antimicrobial screening, *Chem. Biol. Drug Des.*, 2018, **91**(4), 915–923.
20 K. D. Katariya, S. R. Shah and D. Reddy, Anticancer, antimicrobial activities of quinoline based hydrazone analogues: Synthesis, characterization and molecular docking, *Bioorg. Chem.*, 2020, **94**, 103406.
21 F. Zhi, *et al.*, Crystal structures and antibacterial activity of hydrazone derivatives from 1 H-indol-3-acetohydrazide, *J. Struct. Chem.*, 2013, **54**, 148–154.
22 V. Velezheva, *et al.*, Synthesis and antituberculosis activity of indole–pyridine derived hydrazides, hydrazide–hydrazones, and thiosemicarbazones, *Bioorg. Med. Chem. Lett.*, 2016, **26**(3), 978–985.
23 M. Siddique, *et al.*, Biological potential of synthetic hydrazide based Schiff bases, *J. Sci. Innov. Res.*, 2013, **2**, 651–657.
24 R. Sreenivasulu, *et al.*, Synthesis, antiproliferative and apoptosis induction potential activities of novel bis (indolyl) hydrazide-hydrazone derivatives, *Bioorg. Med. Chem.*, 2019, **27**(6), 1043–1055.
25 F. D. Guilherme, *et al.*, Synthesis, chemical characterization and antimicrobial activity of new acylhydrazones derived from carbohydrates, *J. Mol. Struct.*, 2019, **1184**, 349–356.
26 S. H. Rohane, *et al.*, Synthesis and in vitro antimycobacterial potential of novel hydrazones of eugenol, *Arabian J. Chem.*, 2020, **13**(2), 4495–4504.
27 M. M. Shakdofa, *et al.*, Metal complexes of hydrazones and their biological, analytical and catalytic applications: A review, *Main Group Chem.*, 2014, **13**(3), 187–218.
28 E. T. Guimarães, *et al.*, Potent immunosuppressive activity of a phosphodiesterase-4 inhibitor N-acylhydrazone in models of lipopolysaccharide-induced shock and delayed-type hypersensitivity reaction, *Int. Immunopharmacol.*, 2018, **65**, 108–118.
29 M. Jakubek, *et al.*, Hydrazones as novel epigenetic modulators: Correlation between TET 1 protein inhibition activity and their iron (II) binding ability, *Bioorg. Chem.*, 2019, **88**, 102809.
30 E. Başaran, *et al.*, Synthesis, structural characterization, and biological evaluation of some hydrazone compounds as potential antioxidant agents, *Russ. J. Bioorg. Chem.*, 2022, **48**(1), 143–152.
31 Y. Fang, *et al.*, Design, synthesis, and biological evaluation of compounds with a new scaffold as anti-neuroinflammatory agents for the treatment of Alzheimer's disease, *Eur. J. Med. Chem.*, 2018, **149**, 129–138.
32 N. Li, *et al.*, Design, synthesis and biological evaluation of novel pyrimidinedione derivatives as DPP-4 inhibitors, *Bioorg. Med. Chem. Lett.*, 2018, **28**(12), 2131–2135.
33 Y. İ. Esmer, E. Çınar and E. Başaran, Design, docking, synthesis and biological evaluation of novel nicotinohydrazone derivatives as potential butyrylcholinesterase enzyme inhibitor, *ChemistrySelect*, 2022, **7**(33), e202202771.
34 R. Çakmak, B. Akış and M. Şentürk, New Sulfonate Ester-Linked Fluorinated Hydrazone Derivatives as Multitarget Carbonic Anhydrase and Cholinesterase Inhibitors: Design, Synthesis, Biological Evaluation, Molecular Docking and ADME Analysis, *Chem. Biodiversity*, 2024, e202401849.
35 F. S. Tokalı, *et al.*, Novel hydrazones derived from anthranilic acid as potent cholinesterases and α-glycosidase inhibitors: Synthesis, characterization, and biological effects, *J. Biochem. Mol. Toxicol.*, 2024, **38**(1), e23521.
36 M. Krátký, *et al.*, Hydrazones of 4-(trifluoromethyl) benzohydrazide as new inhibitors of acetyl-and butyrylcholinesterase, *Molecules*, 2021, **26**(4), 989.
37 F. S. Tokalı, *et al.*, Synthesis, characterization, bioactivity impacts of new anthranilic acid hydrazones containing aryl sulfonate moiety as fenamate isosteres, *ChemistrySelect*, 2023, **8**(13), e202300241.
38 A. Kamalı, R. Çakmak and M. Boğa, Anticholinesterase and antioxidant activities of novel heterocyclic Schiff base derivatives containing an aryl sulfonate moiety, *J. Chin. Chem. Soc.*, 2022, **69**(4), 731–743.
39 E. Başaran, *et al.*, Combined experimental and theoretical analyses on design, synthesis, characterization, and in vitro cytotoxic activity evaluation of some novel imino derivatives containing pyrazolone ring, *J. Mol. Struct.*, 2022, **1265**, 133427.
40 R. Çakmak, Synthesis and in vitro human carbonic anhydrase I and II inhibition properties of some novel hydrazone compounds containing an aryl sulfonate moiety, *Erzincan Univ. J. Sci. Technol.*, 2020, **15**(2), 659–669.

41 E. Başaran, Schiff base derivatives based on ampyrone as promising acetylcholinesterase inhibitors: Synthesis, spectral characterization, biological activity, and SwissADME predictions, *Russ. J. Bioorg. Chem.*, 2023, **49**(1), 114–126.
42 M. A. Omar, *et al.*, Hydrazone–sulfonate hybrids as potential cholinesterase inhibitors: design, synthesis and molecular modeling simulation, *Future Med. Chem.*, 2023, **15**(24), 2269–2287.
43 X. Gao, J. Tang, H. Liu, L. Liu and Y. Liu, Structure–activity study of fluorine or chlorine-substituted cinnamic acid derivatives with tertiary amine side chain in acetylcholinesterase and butyrylcholinesterase inhibition, *Drug Dev. Res.*, 2019, **80**(4), 438–445.
44 Q. Lu, Y. Chen, H. Liu, J. Yan, P. Cui, Q. Zhang and Y. Liu, Nitrogen-containing flavonoid and their analogs with diverse B-ring in acetylcholinesterase and butyrylcholinesterase inhibition. Drug Development Research, *Drug Dev. Res.*, 2020, **81**(8), 1037–1047.
45 P. Singh, *et al.*, An 18 kDa TSPO specific ligand-based polymeric nanoformulation: synthesis, computational and biological studies, *New J. Chem.*, 2024, **48**(21), 9498–9513.
46 M. G. Kurban, *et al.*, Synthesis of new sulfonamide derivatives: Investigation of their interactions with carbonic anhydrase and cholinesterase enzymes by in vitro and in silico evaluations, *J. Mol. Struct.*, 2024, 138798.
47 A. Korkmaz and E. Bursal, Synthesis, biological activity and molecular docking studies of novel sulfonate derivatives bearing salicylaldehyde, *Chem. Biodiversity*, 2022, **19**(6), e202200140.
48 Y. Demir, *et al.*, Morpholine-modified thiosemicarbazones and thiazolidin-4-ones against Alzheimer's key enzymes: From synthesis to inhibition, *Comput. Biol. Chem.*, 2026, **120**, 108683.
49 F. S. Tokalı, *et al.*, Design and synthesis of new thienopyrimidine derivatives as potential anticancer agents: From cytotoxicity screening to VEGFR inhibition modeling, *J. Mol. Struct.*, 2026, **1352**, 144425.
50 Z. Arslan, *et al.*, Detection and in silico evaluation of undeclared venlafaxine and clomethiazole in a counterfeit herbal product marketed for alcohol withdrawal syndrome, *J. Pharm. Biomed. Anal.*, 2026, **268**, 117189.
51 H. Aftab, *et al.*, A series of 4-thiomorpholinophenyl-thiosemicarbazones as cholinesterase inhibitors with anti-neuroblastoma effects, *Bioorg. Chem.*, 2026, **168**, 109364.
52 W. S. Qayed, *et al.*, 2-Oxoindolin-thiazoline hybrids as scaffold-based therapeutics for T2DM-associated cognitive impairment: design, synthesis, in vitro and in silico studies, *RSC Med. Chem.*, 2026, **17**, 317–342.
53 F. S. Tokalı, *et al.*, Exploring highly selective polymethoxy fenamate isosteres as novel anti-prostate cancer agents: Synthesis, biological activity, molecular docking, molecular dynamics, and ADME studies, *J. Mol. Struct.*, 2025, **1319**, 139519.
54 A. Farzaliyeva, *et al.*, Synthesis and biological studies of acetophenone-based novel chalcone, semicarbazone, thiosemicarbazone and indolone derivatives: Structure-Activity relationship, molecular docking, molecular dynamics, and kinetic studies, *J. Mol. Struct.*, 2025, **1321**, 140197.
55 G. Çelik Turgut, *et al.*, Therapeutic Potential of Nitrogen-Substituted Oleanolic Acid Derivatives in Neuroinflammatory and Cytokine Pathways: Insights From Cell-Based and Computational Models, *Chem. Biodiversity*, 2025, e202500269.
56 U. A. Muhammad, *et al.*, Synthesis of benzimidazole based hydrazones as non-sugar based α-glucosidase inhibitors: structure activity relation and molecular docking, *Drug Dev. Res.*, 2021, **82**(7), 1033–1043.
57 H. Şenol, *et al.*, Synthesis of new fatty acid derivatives of oleanane and ursane triterpenoids and investigation of their in vitro cytotoxic effects on 3T3 fibroblast and PC3 prostate cancer cell lines, *Org. Commun.*, 2020, **13**(3), 114–126.
58 B. Zengin Kurt, *et al.*, Synthesis of Sorafenib−Ruthenium Complexes, Investigation of Biological Activities and Applications in Drug Delivery Systems as an Anticancer Agent, *J. Med. Chem.*, 2024, **67**(6), 4463–4482.
59 G. L. Ellman, *et al.*, A new and rapid colorimetric determination of acetylcholinesterase activity, *Biochem. Pharmacol.*, 1961, **7**(2), 88–95.
60 S. Kermaninia, *et al.*, Novel diazen-bis (phenoxy-1, 2, 3-triazole-N-phenylacetamide) derivatives as potent anti-cholinesterase and anti-α-amylase agents: in vitro and in silico evaluations, *J. Mol. Struct.*, 2025, 143490.
61 M. Noori, *et al.*, Rhodanine-pyridinium derivatives as a new category of cholinesterase inhibitors: Design, synthesis, in vitro and in silico enzymatic evaluations, *Int. J. Biol. Macromol.*, 2025, **320**, 145731.
62 S. Bardaweel, *et al.*, Design, synthesis, and biological evaluation of novel MAO-A inhibitors targeting lung cancer, *Molecules*, 2022, **27**(9), 2887.
63 N. K. Nandi, *et al.*, Design, synthesis, pharmacological and in silico screening of disubstituted-piperazine derivatives as selective and reversible MAO-A inhibitors for treatment of depression, *J. Mol. Struct.*, 2023, **1276**, 134671.
64 Y. Qin, *et al.*, A novel colorimetric lead ion detection method using lead-2′ 3-dimercaptosuccinic acid chelates to catalyze etching of gold nanostars, *Sens. Actuators Rep.*, 2025, **10**, 100351.
65 Z. Narmuratova, *et al.*, Equine lactoferrin: Antioxidant properties related to divalent metal chelation, *LWT*, 2022, **161**, 113426.
66 F. Benchikh, *et al.*, Free radical scavenging, metal chelating and antiperoxidative activities of M. communis berries methanol extract and its fractions, *Turk. J. Agric. Food Sci. Technol.*, 2022, **10**(6), 1089–1094.
67 B. Zengin Kurt, *et al.*, Exploring anticancer properties of new triazole-linked benzenesulfonamide derivatives against colorectal carcinoma: Synthesis, cytotoxicity, and in silico insights, *Bioorg. Med. Chem.*, 2025, **119**, 118060.
68 E. N. Ay, *et al.*, Synthesis, characterization, In vitro and In silico investigations of novel 1,2,3-triazole substituted salicylic acid phenolic hydrazones hybrids targeting TGF-β2 expression in colorectal carcinoma, *Eur. J. Med. Chem.*, 2025, **296**, 117915.